

Scalable DAQ system operating the CHIPS-5 neutrino detector

Belén Alonso Rancurel², Nicolas Angelides⁵, Guillaume Augustoni², Simeon Bash^{1,†} , Benedikt Bergmann³ , Nicholas Bertschinger⁴, Paul Bizouard¹, Medbh Campbell¹, Son Cao¹⁹ , Thomas J. Carroll⁴, Rhys Castellán¹, Erika Catano-Mur¹⁴ , John P. Cesar¹² , João A. B. Coelho²² , Patrick Dills²⁸, Thomas Dodwell¹, Jack Edmondson¹, Daan van Eijk⁷, Quinn Fetterly⁴, Zoé Garbal², Stefano Germani^{1,23}, Thomas Gilpin¹, Anthony Giraud², Alec Habig¹¹ , Daniel Hanuska⁴, Harry Hausner⁹ , Wilson Y. Hernandez⁴, Anna Holin²⁰ , Junting Huang¹⁸, Sebastian B. Jones¹ , Albrecht Karle¹⁶ , George Kileff¹, Kai R. Jenkins¹, Paul Kooijman⁷, Arthur Kreymer⁹ , Gabe M. LaFond⁴, Karol Lang¹² , Jeffrey P. Lazar¹⁶ , Rui Li¹⁰, Kexin Liu^{24,25}, David A. Loving¹⁴, Petr Mánek^{*,1,3} , Marvin L. Marshak¹³ , Jerry R. Meier¹³, William Miller¹³, Jeffrey K. Nelson¹⁴ , Christopher Ng²⁷, Ryan J. Nichol¹ , Vittorio Paolone²¹ , Andrew Perch¹, Maciej M. Pfützner¹, Alexander Radovic^{1,14}, Katherine Rawlins⁸, Patrick Roedl⁴, Lucas Rogers⁴, Ibrahim Safa¹⁵ , Alexandre Sousa¹⁷ , Josh Tingey¹ , Jennifer Thomas¹ , Jozef Trokan-Tenorio¹⁴, Patricia Vahle¹⁴ , Richard Wade⁶, Christopher Wendt⁴ , Daniel Wendt²⁶, Leigh H. Whitehead^{1,‡} , Samuel Wolcott⁴, Tianlu Yuan¹⁶ 

- 1 Department of Physics and Astronomy, University College London, Gower Street, London, WC1E 6BT, United Kingdom
- 2 Aix-Marseille University, Science Faculty in Saint-Jérôme campus, 13013 Marseille, France
- 3 Institute of Experimental and Applied Physics, Czech Technical University in Prague, Husova 240/5, 110 00 Prague, Czech Republic
- 4 Department of Physics, University of Wisconsin, Madison, WI 53706, United States
- 5 Imperial College London, Physics Department, Blackett Laboratory, London SW7 2AZ, United Kingdom
- 6 Avenir Consulting, Abingdon, Oxfordshire, United Kingdom
- 7 Nikhef, Science Park 105, 1098 XG, Amsterdam, Netherlands
- 8 University of Alaska Anchorage, 3211 Providence Dr. Anchorage, AK 99508, United States
- 9 Fermi National Accelerator Laboratory, Batavia, IL 60510, United States
- 10 School of Physics and Astronomy, Shanghai Jiao Tong University, MOE Key Laboratory for Particle Astrophysics and Cosmology, Shanghai Key Laboratory for Particle Physics and Cosmology, Shanghai 200240, China
- 11 Department of Physics and Astronomy, University of Minnesota Duluth, Duluth, MN 55812, United States
- 12 Department of Physics, University of Texas at Austin, Austin, TX 78712, United States
- 13 University of Minnesota, Minneapolis, MN 55455, United States
- 14 Department of Physics, William & Mary, Williamsburg, VA 23187, United States
- 15 Department of Physics, Columbia University, New York, NY, United States
- 16 Department of Physics and Wisconsin IceCube Particle Astrophysics Center, University of Wisconsin–Madison, Madison, WI 53706, United States
- 17 Department of Physics, University of Cincinnati, Cincinnati, OH 45221, United States
- 18 School of Physics and Astronomy, Shanghai Jiao Tong University, China
- 19 Institute For Interdisciplinary Research in Science and Education, ICISE, Quy Nhon, Vietnam
- 20 Particle Physics Department, STFC Rutherford Appleton Laboratory, Harwell Campus, Didcot OX11 0QX, United Kingdom
- 21 University of Pittsburgh, Pittsburgh, PA 15260, United States
- 22 Université Paris Cité, Astroparticule et Cosmologie, F-75013 Paris, France
- 23 Dipartimento di Fisica e Geologia, Università degli Studi di Perugia, I-06123 Perugia, Italy
- 24 Department of Physics, Sun Yat-sen University, 135 Xingang Xi Road, Haizhu District, Guangzhou 510275, China
- 25 Department of Physics, Tsinghua University, 30 Shuangqing Road, Haidian District, Beijing 100084, China
- 26 Department of Physics, University of Colorado, Boulder, CO 80309, United States
- 27 Department of Physics and Astronomy, Michigan State University, East Lansing, MI 48824, United States
- 28 Department of Mechanical Engineering, University of Wisconsin, Madison, WI 53706, United States
- * Correspondence: petr.maneck.19@ucl.ac.uk
- † Now at Technische Universität München, James-Frank-Straße, 85748 Garching, Germany
- ‡ Now at Cavendish Laboratory, University of Cambridge, Cambridge CB3 0HE, United Kingdom

Abstract: The CHIPS R&D project focuses on development of low-cost water Cherenkov neutrino detectors through novel design strategies and resourceful engineering. This work presents an end-to-end DAQ solution intended for a recent 5 kt CHIPS prototype, which is largely based on affordable mass-produced components. Much like the detector itself, the presented instrumentation is composed of modular arrays that can be scaled up and easily serviced. A single such array can carry up to



Citation: Mánek P. et al. Scalable DAQ system operating the CHIPS-5 neutrino detector. *Preprints* 2024, 1, 0. <https://doi.org/>



Copyright: © 2024 by the authors. Licensee MDPI, Basel, Switzerland. This article is an open access article distributed under the terms and conditions of the Creative Commons Attribution (CC BY) license (<https://creativecommons.org/licenses/by/4.0/>).

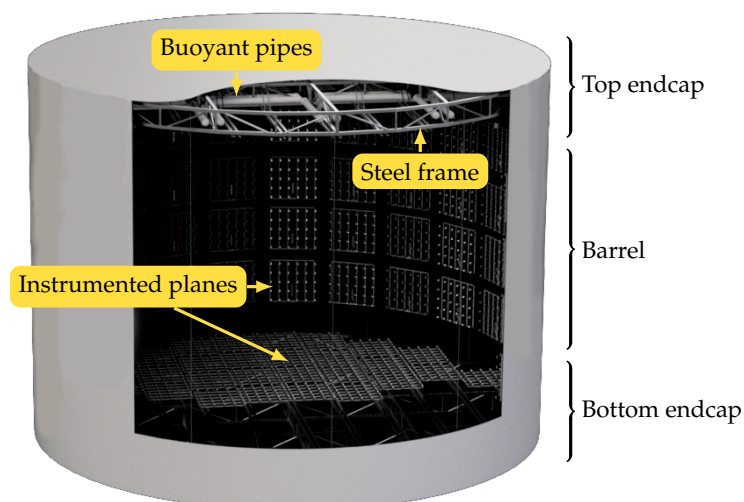


Figure 1. Rendering of CHIPS-5 in its fully deployed state, courtesy of T. Dodwell.

30 photomultiplier tubes (PMTs) accompanied by electronics that generate high voltage in-situ and deliver time resolution of up to 0.69 ns. In addition, the technology is compatible with the White Rabbit timing system, which can synchronize its elements to within 100 ps. While deployment issues did not permit the presented DAQ system to operate beyond initial evaluation, the presented hardware and software successfully passed numerous commissioning tests that demonstrated their viability for use in a large-scale neutrino detector, instrumented with thousands of PMTs.

Keywords: neutrino detector; water Cherenkov detector; data acquisition; photomultiplier tube; parallel processing

1. Introduction

Experiments studying neutrinos address low signal rates by constructing massive detectors that can collect statistically significant data within acceptable time frame. Building a large apparatus on the scale of tens or hundreds of kilotons, however, poses a series of unique challenges that call for large research collaborations and prohibitively substantial upfront investments. The Cherenkov Detectors in Mine Pits (CHIPS) R&D project [1] sidesteps many such issues by developing low-cost neutrino detector technology based on affordable mass-produced components. CHIPS-style detectors employ modular architecture, which allows them to be readily constructed at small scale and expanded on demand, easily serviced, and operated at multiple locations to observe coincident events with sub-nanosecond time resolution.

To demonstrate and verify this concept, CHIPS tested a number of detector prototypes over the last decade. The latest and largest one to date was CHIPS-5, which was realized between 2018 and 2020 [2]. CHIPS-5 (pictured in Figure 1) was a 5.9 kt water Cherenkov detector that comprised a cylindrical tank, 12 m tall and 25 m across, which was deployed underwater in a disused mining pit near Hoyt Lakes, Minnesota, 7 mrad off axis of the NuMI neutrino beam [3]. This location allowed CHIPS-5 to study neutrino oscillations by probing ν_μ disappearance over a 712 km baseline, as illustrated in Figure 2.

Modular aspects of CHIPS-5's architecture were by no means limited only to its structural elements. The detector in its entirety was designed to be expandable, so that its technology may be used in larger-scale deployments without significant alteration. To this end, its photosensitive instrumentation was organized into planar optical modules (POMs) – segmented arrays of photomultiplier tubes (PMTs) that were mounted on its internal surface. Each POM was an autonomous measuring unit that in addition to PMTs carried electronics

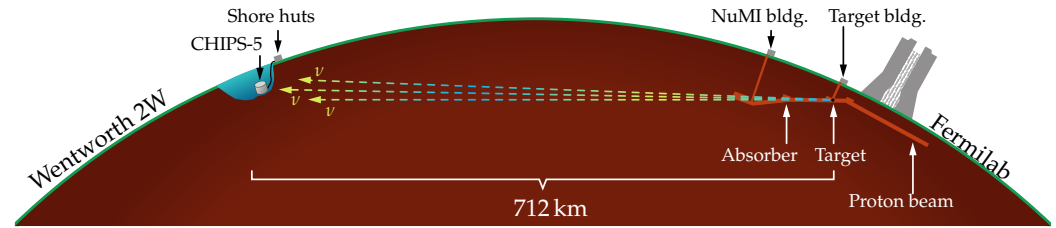


Figure 2. Intended operation of CHIPS-5 in the path of the NuMI neutrino beam (not to scale). Neutrinos generated at Fermilab (right) travel through Earth’s crust to emerge at the Wentworth 2W mining pit, where CHIPS-5 was deployed (left).

for high voltage generation, time synchronization and pulse digitization. Interlinked POMs gave rise to a network that was controlled by dedicated software, which aggregated data and performed clustering in real-time. Together, these components formed a data acquisition (DAQ) system, which facilitated flow of data from PMTs to a persistent storage facility at Fermilab.

While it is infeasible to give a full account of the detector design details in the scope of a single article, this work aims to provide an overview of its functional components with principal focus on the DAQ system. The rest of the text is therefore structured as follows. Section 2 is devoted to low-level electronics, such as PMTs and POMs, which were responsible for digitizing and timestamping measurements. Next, Section 3 discusses infrastructure that distributed power, data links and precise timing signals to all elements of the system. Section 4 is devoted to the software component of the DAQ system, which serviced the hardware, interacted with operators and performed data analysis. Finally, Section 5 summarizes outcomes of the CHIPS-5 deployment and future prospects of its DAQ technology.

2. Measurement hardware

Even though CHIPS-5’s instrumentation shared the same basic structure and purpose, its hardware was not homogeneous. POMs were divided into two functionally equivalent groups, labeled by their institutes of origin: Nikhef and University of Wisconsin, Madison. While Nikhef POMs incorporated electronics that were already in use at the KM3NeT experiment, Madison POMs were seen as a proving ground for a modern PMT readout system developed by CHIPS in collaboration with Wisconsin IceCube Particle Astrophysics Center (WIPAC). This permitted the newer Madison electronics to be qualified by comparison with a well-characterized Nikhef system. Under full instrumentation, CHIPS-5 was designed to hold 226 Nikhef POMs and 30 Madison POMs.

Irrespective of their underlying technology, POMs observed photons through PMTs, which produced analog pulses corresponding to registered light. POM hardware was therefore mainly responsible for supplying PMTs with high voltage, which determined their gain, and digitizing their pulses. Since thousands of PMTs were planned to be instrumented, hardware servicing a single channel needed to remain relatively small and inexpensive. This motivated a tree-shaped architecture, where the lowest-level elements were plain, mass-produced circuit boards. At higher levels of the tree, components became more sophisticated and less numerous, as they aggregated data from lower stages. In addition, timing played a critical role. To be able to correlate hits between multiple channels, digitization mechanism required precise synchronization throughout the entire system. Considering detector dimensions, light was expected to traverse its entire volume within approximately 83.4 ns. This set the time synchronization target to be on the order of nanoseconds, so that sources of Cherenkov light may be accurately localized.

Parameter	HZC XP82B20FNB [4]	Hamamatsu R6091 [6]
Diameter, length	88 mm, 95 mm	76 mm, 137 mm
Gain	1×10^7	5×10^6
Anode pulse rise time	3.5 ns	2.6 ns
Quantum efficiency at 400 nm	24.4 %	12.0 %
Typical (max) anode dark current	20 nA (300 nA)	10 nA (60 nA)

Table 1. Selected parameters of PMTs, which were used in CHIPS-5.

2.1. Photomultiplier tubes

At the lowest level of the DAQ system, CHIPS-5 used two distinct PMT models that aligned with POM types. Their relevant parameters are listed in Table 1. Nikhef POMs used the XP82B20FNB model manufactured by HZC, a Chinese company that recently acquired the photomultiplier division of Photonis. These PMTs had a domed photocathode and measured approximately 88 mm in diameter [4]. In contrast, Madison POMs carried Hamamatsu R6091 PMTs, which were donated from the NEMO-3 experiment [5]. Their photocathode was flat and approximately 76 mm across [6]. Both PMT models were selected to offer acceptable response around 400 nm, which was the estimated wavelength of expected Cherenkov light from neutrinos.

Under normal operation PMTs required steady supply of high voltage in the range of 1.0 kV to 2.5 kV. Since this potential was proportional to gain, it was desirable to adjust it for each channel independently in order to equalize response across the entire detector. In addition, it was viewed as hazardous to distribute high voltages underwater from a centralized supply. PMTs were therefore fitted with bases that generated high voltage in-situ using a Cockroft-Walton (CW) voltage multiplier [7]. This way, power lines could supply PMTs with much safer low-voltage direct current, which was switched and modulated by electronics into high voltages just prior to consumption.

Even though both PMT models shared similar characteristics, their installation in CHIPS-5 required distinct treatment due to differences in polarity. Hamamatsu PMTs were wired with anodes at high voltage and photocathodes close to ground, which permitted the photocathodes to be directly exposed to pit water without any undesirable effects. In contrast, HZC PMTs used inverted configuration with photocathodes at high voltage, which would introduce additional noise into measurements if left unaddressed. For that reason, HZC photocathodes were electrically insulated from surrounding water by transparent acrylic shields that were installed during potting. In the course of this procedure, a gelatinous compound was injected into 0.5 mm gap between a PMT and its shield, and left to harden. To minimize light losses due to reflection and refraction at the optical interface, the compound was selected to match refractive indices of adjacent materials, and the procedure was performed under vacuum that removed any bubbles. A dedicated workflow was devised to efficiently pot batches of PMTs in groups of 155.

In final stages of installation PMTs were mechanically affixed to POMs by plastic inserts that formed water-tight seals with their PVC tubing. To prevent water ingress in photocathode area, PMTs underwent different procedures based on their model. HZC PMT cases were designed to completely enclose their PMTs, so inserts covered the entire tube and interfaced with its acrylic shield by means of o-rings and screws. In contrast, Hamamatsu PMT cases were designed to leave photocathodes exposed, so they were permanently attached to the rim of the tube by water-resistant sealant. Figure 3 shows completed assemblies for both PMT models.

2.2. Nikhef POMs

POMs of the Nikhef type were the most abundant in the DAQ system. In the first phase of CHIPS-5 deployment, both detector endcaps were instrumented with 226 Nikhef POMs carrying 6114 PMTs. Of this number, 324 PMTs located in the top endcap were



(a) PMTs with bases before waterproofing (b) PMTs inside cases, ready for installation
Figure 3. Waterproofing of PMTs before their installation in POMs. Photographs show PMTs manufactured by HZC (left) and Hamamatsu (right) before and after the procedure. Note the domed acrylic shield on the HZC PMT that insulates its photocathode.

oriented upward to observe the veto region and assist with cosmic background rejection. The rest were oriented into the inner volume.

Each Nikhef POM measured approximately $2\text{ m} \times 3\text{ m}$ and carried up to 30 HZC PMTs, which were driven by electronics developed for the KM3NeT project [8,9]. These components can be viewed as two specific groups: application-specific integrated circuits (ASICs) that were embedded in PMT bases, and printed circuit boards (PCBs) that were installed in a cylindrical container in the middle of the POM. Under normal operation data flowed from ASICs to PCBs, which aggregated measurements from the entire POM and transmitted them upstream to higher stages of the DAQ system.

A base of an HZC PMT is shown in Figure 4. Its high voltage was generated by an ASIC known as CoCo (Cockroft-Walton Multiplier Feedback Control) [10]. This circuit produced periodic pulses of frequencies up to 50 kHz that drove a CW voltage multiplier. As its name suggests, CoCo included a sensing feedback mechanism that allowed it to adaptively regulate voltage, so that stable PMT gain could be maintained at desired levels over extended periods of time.

CoCo was configured by a second ASIC called PROMiS (PMT Read Out Mixed Signal) [10], which acted as a main point of communication for a single PMT. PROMiS responded to slow control commands over I²C bus and produced data as low-voltage differential signal (LVDS). Internally PROMiS generated two voltages, adjustable with 8-bit depth: a high voltage control signal that was routed to CoCo, and a threshold voltage that controlled trigger sensitivity. PROMiS used a self-triggering mechanism that continuously compared amplified analog pulse from PMT anode to the configured threshold voltage, and issued triggers whenever pulse amplitude exceeded threshold for the first time. Incoming trigger initiated pulse digitization, which was performed by counting clock cycles until the amplitude of the pulse dropped below the threshold voltage, as illustrated in Figure 5. This gave rise to a quantity known as Time over Threshold (ToT), which was registered with time resolution below 2 ns and represented a single PMT hit. The shortest supported time between two successive hits was 25 ns, which could be viewed as dead time of this technology.

PROMiS encoded ToT data into pulse-width modulated (PWM) LVDS signals, and transmitted them to a Calamares board [11]. Since PROMiS was located in a PMT base and Calamares resided several meters away in a container in the middle of the POM, connection between the two was facilitated by a standard Category 5 (Cat 5) twisted-pair cable [12]. Due to their abundant use in modern networking and telecommunications, these cables were easy to handle, inexpensive and readily available in large quantities. Succeeding an older PCB called Octopus, Calamares acted as a hub for the entire POM. With a distinctive elongated form factor, a pair of Calamares boards was able to accept up

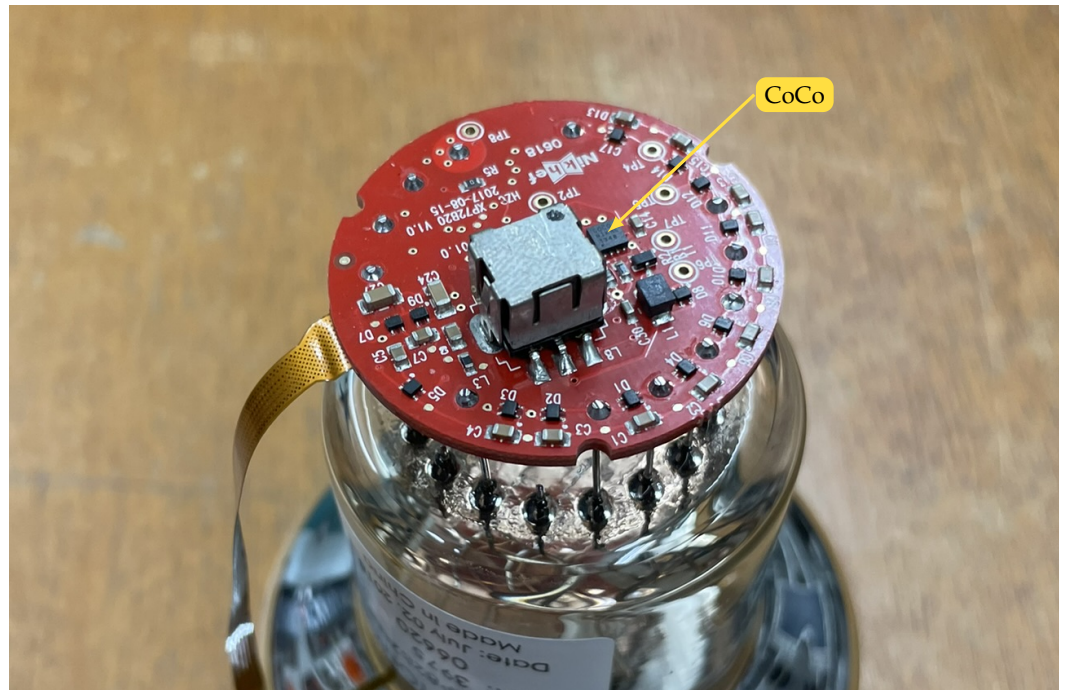


Figure 4. High voltage base of a HZC PMT carrying ASICs. While CoCo is visible in the photograph, PROMiS is fitted on the underside, out of view.

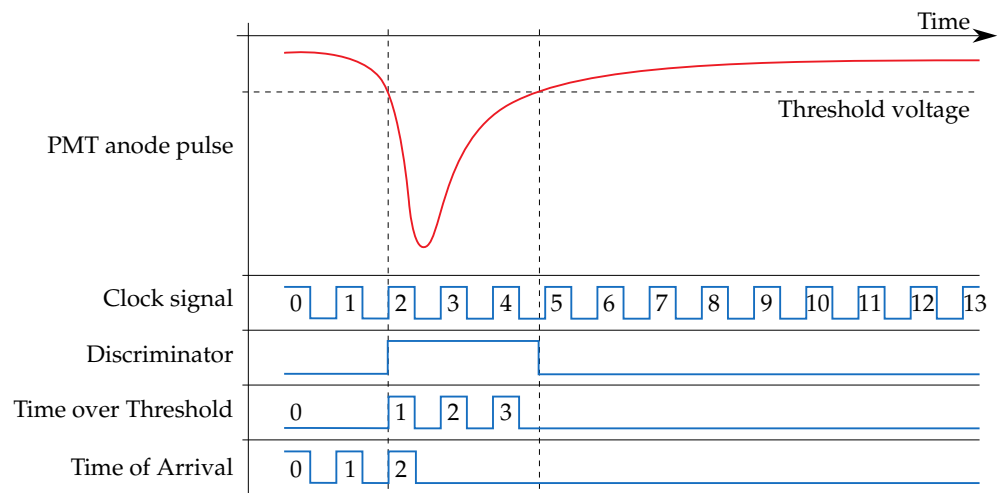


Figure 5. Digitization of an analog pulse using Time over Threshold (ToT) and Time of Arrival (ToA). A discriminator compares analog pulse (red, not to scale) is to an adjustable threshold voltage. While ToT counts the number of clock cycles spent in excess of the threshold, ToA latches the latest timestamp when threshold is exceeded for the first time. In this example, the output ToA is 2 and ToT is 3.

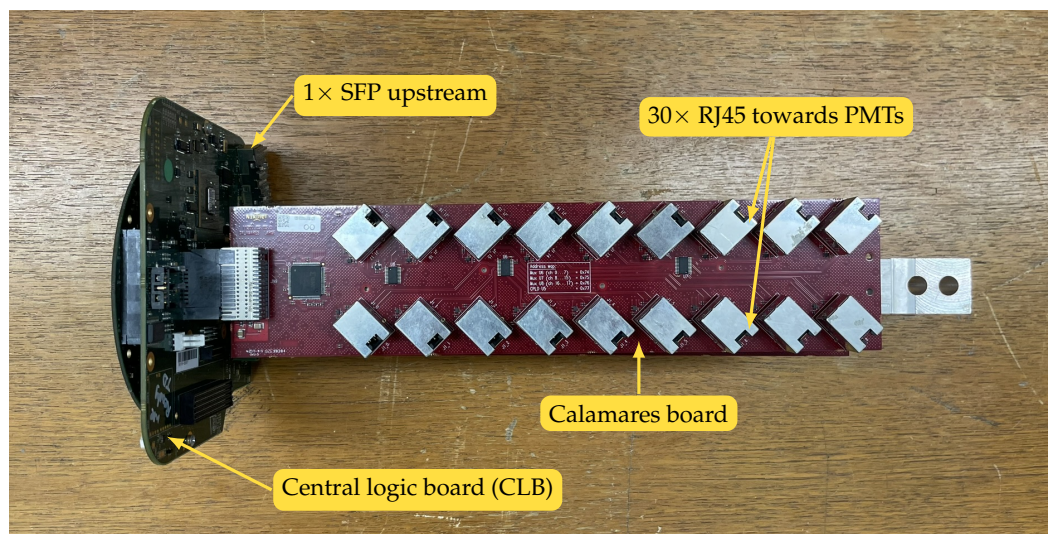


Figure 6. A CLB with a pair of Calamares boards. Note that one Calamares board obscures another board on the underside. Upstream and downstream ports are annotated.

to 30 RJ45 connections from PMT bases. Their main responsibility was to distribute power, clock signals and multiplex I²C communication.

As Figure 6 shows, Calamares interfaced with a Central Logic Board (CLB) [11], which acted as the main point of contact for the POM. CLB was primarily responsible for aggregating measurements from all PMTs of the POM. For each channel, it decoded signals from PROMiS and timestamped them with a 10 MHz clock signal, complementing hit ToT with a quantity called Time of Arrival (ToA). To maintain synchronization with the rest of the detector, the field-programmable gate array (FPGA) inside CLB continuously disciplined its on-board oscillator using methods described in Section 3.1. In addition to processing PMT hits, CLB controlled a flasher circuit known as Nanobeacon [13], which was capable of driving a light-emitting diode (LED) in constant phase with timestamping clock. Nanobeacon delivered light pulses with tunable frequency and intensity, allowing PMTs to be precisely calibrated inside the detector following its deployment. Upstream communication from a CLB was facilitated by a fibre optic 1 Gbit Ethernet link towards fanout electronics containers, which forwarded data to DAQ computers.

CLB together with Calamares boards were installed in a cylindrical pressure-resistant container manufactured from aluminum, which is shown in Figure 7. This compartment received downstream Cat 5 cables from PMTs and upstream data fibres and power lines from higher levels of the DAQ system. Besides PCBs the container also carried a small power supply (PSU) that stepped 240 V down to 12 V for POM electronics. To prevent water ingress into the container, all openings were fitted with waterproof feedthroughs. Similar features were installed throughout the POM near each PMT, dividing pipes into compartments that could independently resist flooding. Figure 8 shows fully assembled Nikhef POMs installed in CHIPS-5.

2.3. Madison POMs

POMs of the Madison type in many aspects mirrored their Nikhef counterparts. For instance, they used the same building elements based on PVC tubing and had approximately similar form factor. Since they were seen as testbeds for the next generation of DAQ electronics, they were only deployed to the bottom endcap of CHIPS-5 and their numbers were relatively limited until thorough commissioning could be conducted. In the initial phase of deployment, the detector was instrumented with 30 Madison POMs carrying 450 PMTs in total. A single Madison POM contained 15 Hamamatsu PMTs, which were driven by novel electronics developed by CHIPS in collaboration with WIPAC [14]. For consistency, these



Figure 7. Partially constructed Nikhef POM with open electronics container, exposing a CLB with Calamares boards. Photograph courtesy of S. Bash.



Figure 8. Fully assembled Nikhef POMs mounted on CHIPS-5 endcaps. On the top endcap, veto PMTs are oriented up. The rest are oriented inward at 45° facing the NuMI beam to maximize light collection. Photograph courtesy of S. Bash.

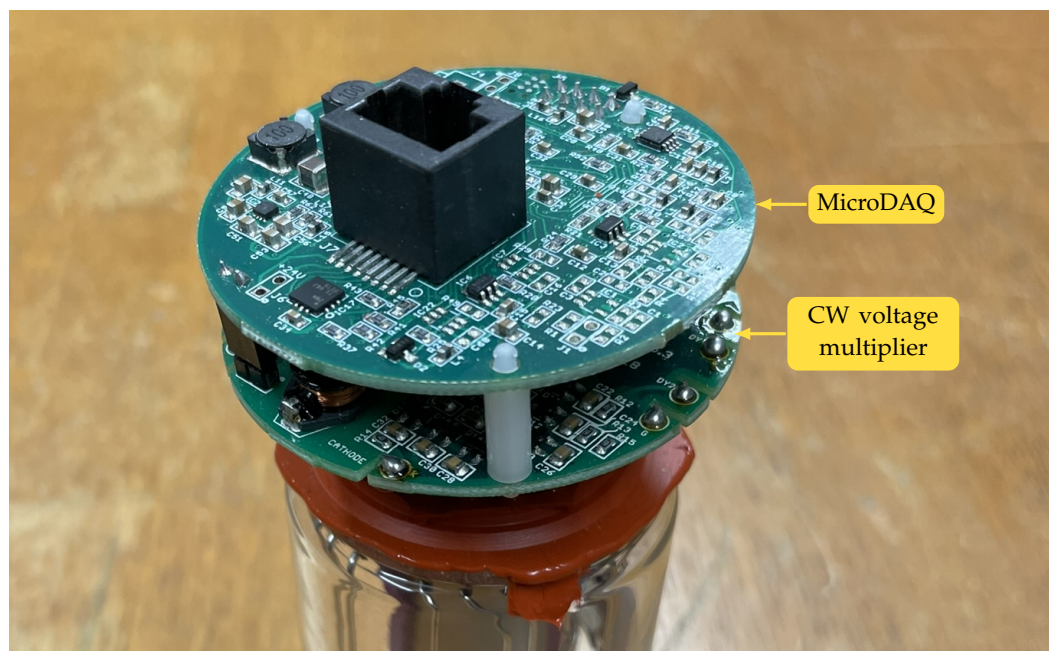


Figure 9. High voltage base of a Hamamatsu PMT. The upper PCB is the MicroDAQ, which is responsible for analog pulse digitization and high voltage control. The lower PCB implements CW voltage multiplier circuit that drives the PMT.

components were organized to match the architecture and data flow of Nikhef hardware. PMT bases were fitted with microcontrollers, which transmitted measurements to a PCB installed in a cylindrical container. From there data travelled upstream towards fanouts, which forwarded it to computers on the shore.

Figure 9 shows the base of a Hamamatsu PMT, which contains a microcontroller circuit called MicroDAQ. This component was the main point of communication for the PMT, and can be functionally viewed as a combination of CoCo and PROMiS. Just like CoCo, MicroDAQ drove a CW voltage multiplier to generate high voltage for the PMT. And just like PROMiS, MicroDAQ amplified and digitized analog pulses from PMT anode. With that said, MicroDAQ implemented several desirable improvements over its counterparts.

Firstly, given its superior computing power the on-board STM32 microcontroller was capable of decoding time signals, which were supplied in the IRIG-B format [15]. This allowed it to assign ToA simultaneously with ToT to each registered hit. In contrast, PROMiS was able to only measure ToT that was later timestamped by a CLB several meters away, subject to cable delay. Secondly, in addition to self-triggering MicroDAQ implemented a CPU trigger that periodically sampled analog pulse regardless of whether threshold was exceeded or not. This permitted a much more accurate characterization of backgrounds. Finally, even though MicroDAQ internally used a 180 MHz clock (corresponds to 5.5 ns period), through resourceful engineering it delivered sub-nanosecond time resolution. This was achieved by routing the analog pulse through a tapped delay line (TDL) with 8 taps, which were latched into registers upon triggering. By comparing contents of these registers, a firmware determined the precise time when threshold was exceeded with resolution of 0.6875 ns without requiring expensive components such as FPGAs or time-to-digital converters (TDCs). This way, MicroDAQs were seen as precision DAQ hardware, which could be manufactured at scale for a price of a conventional PCB, consistent with CHIPS methodology.

MicroDAQ accumulated measurements in a volatile hit buffer that was divided into 32 pages. Under normal operation, contents of these pages were extracted by a PCB known as Badger board, which was located inside a dedicated plastic container in the middle of

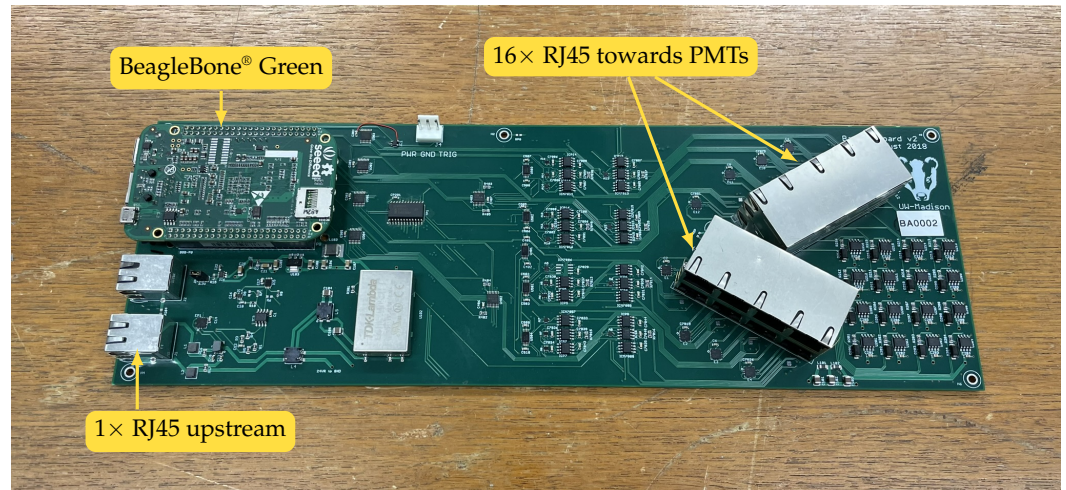


Figure 10. Badger board with BeagleBone® Green SBC. Upstream and downstream ports are annotated.

the POM. Similarly to Nikhef instrumentation, connection between these two elements was facilitated by standard Cat 5 cabling that carried LVDS communications over distances of several meters. However, here data was transmitted over standard RS-232 serial link [16].

A Badger board is shown in Figure 10. Much like Calamares boards with a CLB, this PCB was designed to aggregate their measurements from all PMTs of the POM, and distribute power and timing signals. To this end it incorporated a single-board computer (SBC) called SeedStudio BeagleBone® Green (abbreviated as BeagleBone) [17], which interfaced with the PCB by a pair of 46-pin headers that routed I²C bus and data links to its general-purpose input/output (GPIO) pins. The BeagleBone ran a customized version of the Linux operating system, which was hosted from a microSD card. In this environment, a suite of C programs known as Field Hub App controlled and read out up to 16 MicroDAQs.

Since hits were already timestamped upon digitization, their processing was considerably simplified. Specifically, the BeagleBone did not need to decode timing signals, which freed up its computing power for preliminary analysis and quality control. Communications upstream were implemented over metallic 100 Mbit Ethernet link. This channel was also used for monitoring and maintenance interventions, which typically entailed remote access over Secure Shell Protocol (SSH).

Just like CLBs, Badger boards were able to drive a single Nanobeacon flasher in synchronization with timestamping clock for the purposes of PMT calibration. Intensity and frequency of delivered pulses were programmed from the BeagleBone over I²C bus. The entire electronics assembly consisting of a single Badger board, a Nanobeacon and a 24 V PSU was enclosed in a plastic cylinder, modelled after its aluminum counterpart from Nikhef POMs. This design, visible in Figure 11, aimed to reduce costs by employing standard PVC plumbing parts with glued joints instead of machined components with feedthroughs.

Madison POMs were waterproofed in similar fashion to Nikhef POMs. PVC tubing was divided by bulkheads into a series of compartments, which were able to resist flooding independently. Thanks to material consistency, PVC glue was generously used along all joints and interfaces. The end result is presented in Figure 12, which shows fully assembled Madison POMs installed in CHIPS-5.

3. Infrastructure hardware

Besides POMs, which represented the bulk of submerged instrumentation, the CHIPS-5 detector also included auxiliary DAQ subsystems that supplied all elements with power, accurate timing and high-speed network links. This equipment represented the infrastruc-



Figure 11. Sealed electronics container of a Madison POM. Inside is a Badger board (middle compartment) with a Nanobeacon (capped pipe on the left). Cat 5 cabling enters the container from the right side. Photograph courtesy of S. Bash.

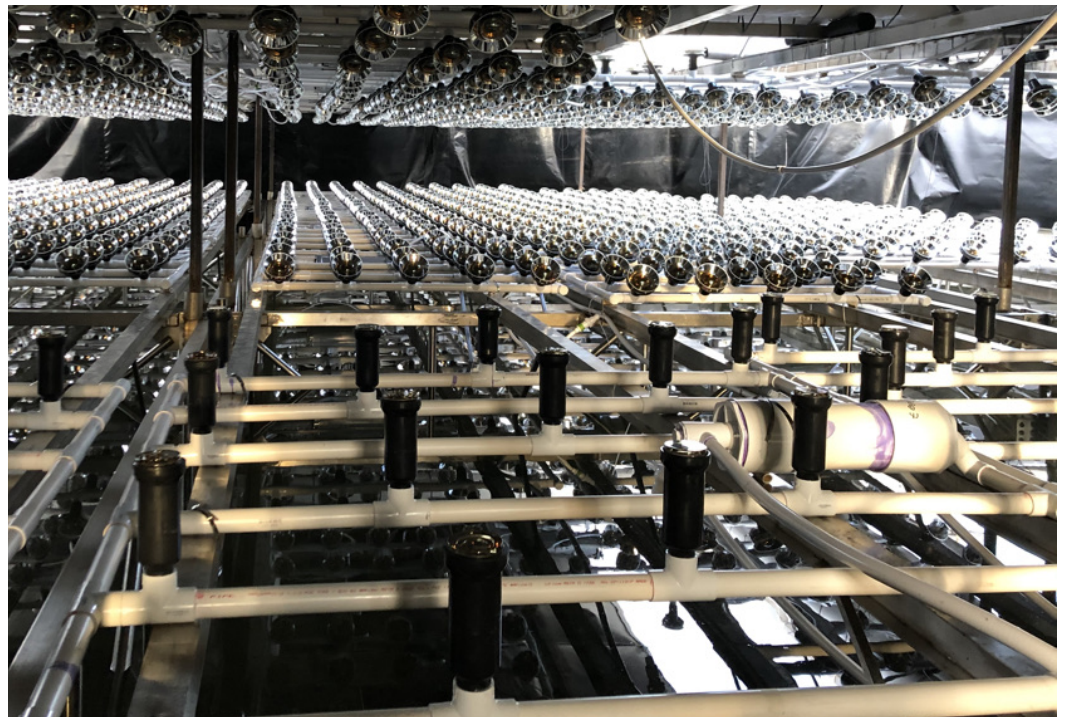


Figure 12. Fully assembled Madison POMs (front) mounted alongside their Nikhef counterparts (back) on CHIPS-5 endcaps. Note that PMT density of Madison POMs is half that of Nikhef POMs. Photograph courtesy of S. Bash.

ture that interconnected submerged devices and patched them to a hut on the shore of the mining pit, where additional hardware was installed. This included mainly computers, network switches, power supplies, relays and timing equipment.

3.1. Time distribution

To ensure that flashes of Cherenkov light were seen as coincident from multiple vantage points, POM instrumentation needed to timestamp PMT hits with a clock that was precisely synchronized to the same reference across the entire detector. Furthermore, given CHIPS-5 dimensions it was critical for this synchronization to be accurate within at least units of nanoseconds. This motivated use of White Rabbit (WR) timing system [18].

Originally developed by the European Organization for Nuclear Research (CERN) between 2008 and 2012, WR is an ongoing research project aiming to deliver sub-nanosecond time synchronization for applications in physics research and industry. At its inception, WR protocol specification as well as its core implementation were made openly available in the public domain, which allowed researchers as well as private companies to freely adopt this technology. Since then many manufacturers have expanded their portfolios to include WR-compatible products. In 2019, thanks to widespread use of WR the protocol was incorporated into the IEEE 1588 standard as the high accuracy profile of Precision Time Protocol (PTP) version 3 [19].

From user perspective, a great advantage of WR is its elegant use of abundant network infrastructure. Instead of requiring specialized cables, hubs or receptacles, the timing system is implemented as an extension of a conventional 1 Gbit Ethernet network carried over single-mode bidirectional optical fibres. This makes WR much more interoperable, as it permits WR-enabled peripherals, also called *WR nodes*, to readily communicate with any other devices regardless of their compatibility. Support for the WR protocol is detected automatically during link negotiation phase and enabled only if implemented by both sides. When enabled, network interface controllers (NICs) of WR nodes regularly exchange time synchronization packets injected into ordinary Ethernet traffic. Since these data frames are immediately consumed by WR hardware on both ends of the link, they are rendered invisible to any software supervising the data exchange. This is highly desirable, as it allows a single fibre to simultaneously carry communications as well as precise time.

While low-level implementation of WR is beyond the scope of this text, its basic operating principle is not difficult to summarize. Both participants of a WR link have oscillators, which can be viewed as local clocks. In their initial state these clocks would inherently drift apart given a sufficient period of time. To prevent this, nodes on both sides exchange messages that establish a phase-locked loop (PLL). This gives rise to a hierarchy where one node, known as the *slave*, perpetually adjusts its clock to match the other, known as the *master*. Since a PLL maintains constant but not necessarily zero phase between clocks, additional messages are continuously exchanged to track and subtract this phase offset. Finally, to counteract delays due to fibre length WR packets are timestamped by their senders, allowing both nodes to measure and subtract roundtrip latency. Accuracy of this measurement can be further improved through a specialized calibration procedure that probes asymmetry of transmit/receive operations of the specific model of small form-factor pluggable transceiver (SFP). When all these approaches are applied in concert, two directly connected WR nodes can typically synchronize their local clocks to within 100 ps over potentially vast physical distances. For instance, in 2021 a WR-based system was able to synchronize clocks between New Jersey and Chicago over the distance of 1350 km with mean offset of 112 ± 139 ps [20].

When WR is deployed over larger networks, the same time synchronization process is repeated for each adjacent pair of WR nodes, forming a chain of mutually synchronized devices. This introduces one practical drawback of this technology: it is usually undesirable to introduce incompatible elements to higher levels of WR networks, as they strip away timing information and prevent it from propagating. Since conventional Ethernet switches would have this exact effect, WR offers its own equivalent network element, known as

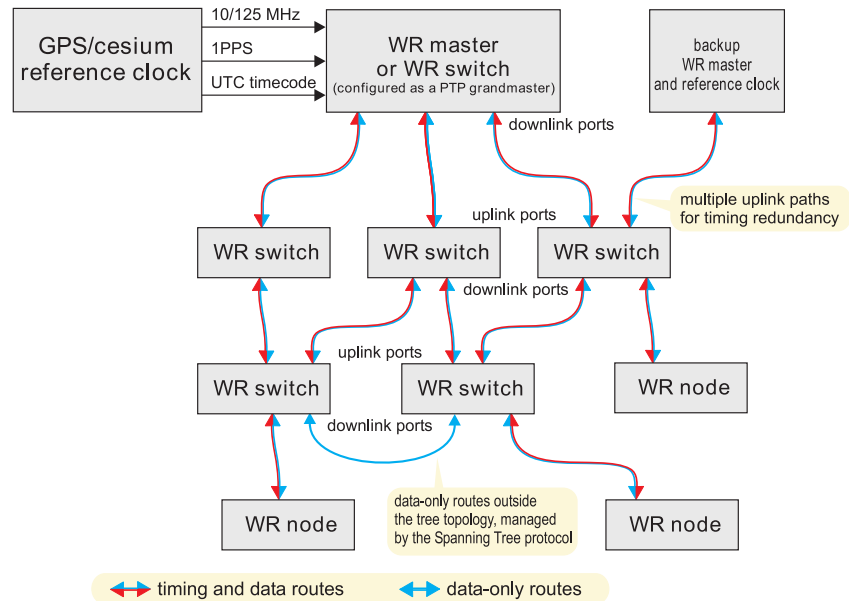


Figure 13. A typical WR network. Time is distributed from a reference clock through a topology of switches down to nodes. Blue-red arrows indicate fibre links, which transmit data as well as timing signals. Diagram taken from reference [18].

WR switch, which acts as a *WR node* on all ports [21]. *WR switches* allow *WR networks* to branch into tree-shaped topologies, where switches at each level act as masters for the level below and slaves for the level above. In addition, these topologies allow for improved reliability where multiple clock sources can offer redundant failover capacity in case of faults. The *WR switch* situated in the root of the tree is called the *grandmaster*, since it distributes its clock to all other nodes in the system. This is topology illustrated in Figure 13.

Grandmasters typically keep their own free-running clocks or receive clock reference from external time sources, such as atomic clocks or Global Navigation Satellite System (GNSS) receivers. *WR switch* hardware expects this information to be supplied as a pair of standardized timing signals:

1. 10 MHz sine wave, which precisely marks time within the scope of a single second.
2. IRIG-B square wave signal of frequency 1 Hz¹, which marks the turnover of a second and encodes time-of-day (ToD) information.

This method represents an attractive option for physics projects such as CHIPS-5, which not only needed to synchronize instrumentation within the scope of the detector, but also aimed to correlate PMT timestamps with spills of the Fermilab accelerator hundreds of kilometres away. Without necessitating a dedicated communications line connecting the two facilities, GNSS receivers could be used on both ends of the baseline to retrieve International Atomic Time (TAI), which was used as a common clock reference. This was fed into grandmaster *WR switches* that synchronized the rest of equipment on site.

3.2. Networking and power infrastructure

At the CHIPS-5 site in Minnesota, *WR* was deployed as a part of broader infrastructure that distributed power and communications from shore equipment to submerged PMTs. This system consisted of several cylindrical containers, which structurally resembled those carried by POMs. While most of them were so-called *fanouts*, which serviced groups of POMs, one container, known as the *junction box*, was the master hub that was patched directly to the umbilical. Interconnections between the *junction box*, *fanouts* and POMs

¹ IRIG-B standard requires complete ToD information to be transmitted every second. However, bits representing this data are sent at 100 Hz. [15]

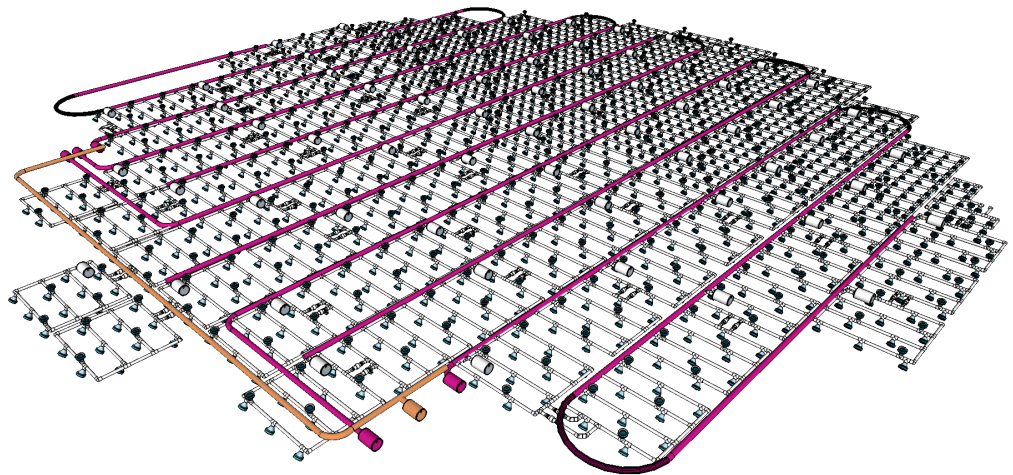


Figure 14. Rendering of the CHIPS-5 top endcap. Nikhef POMS (white) are interconnected by manifolds (orange, pink). Picture courtesy of T. Dodwell.



(a) Commercially available WR switch. [23] **(b)** Compact WR switch used by CHIPS-5. [22]
 Dimensions: 447 mm × 44 mm × 223 mm Dimensions: 75 mm × 47 mm × 236 mm

Figure 15. WR switch comparison illustrating benefits of a compact PCB developed by Nikhef (b) over a commercially available solution (a). Pictures are not to scale.

were facilitated by elaborate conduits called *manifolds*, which protected cables and optical fibres inside waterproof PVC hoses. These are illustrated in Figure 14.

Fanouts were responsible for power switching and multiplexing WR network towards a group of POMS. Since their technology depended on POMS, there existed two types of fanouts that aligned with POM types. In its initial phase of deployment, CHIPS-5 was equipped with 5 Nikhef fanouts and 1 Madison fanout.

Nikhef fanouts contained a pair of WR switches, which were cross-linked for redundancy. In the upstream direction, these switches were patched to shore huts through the junction box. In the downstream direction, they interacted directly with CLBs on-board Nikhef POMS. Since CLBs were programmed as WR slaves, they were able to access precise time as well as data links for DAQ and detector control. Besides WR switches Nikhef fanouts also carried network-controlled relay boards, which interrupted power to individual POMS on remote command. To adapt metallic links from relay boards and WR switch management interfaces to optical fibres, media converters were installed inside fanout containers.

During assembly of Nikhef fanouts, an interesting challenge was presented by large dimensions of WR switches. Since these network elements were normally designed to operate in standard 19 in wide telecommunications racks, their commercially available enclosures were unsuitable for confined fanout containers. To overcome this issue and maximize packing efficiency, Nikhef developed a PCB that was functionally equivalent to a WR switch, but had considerably smaller footprint [22]. Figure 15 shows how this device compares to a commercial WR switch.

Much like their Nikhef counterparts, Madison fanouts were responsible for distributing communications and power to up to 16 Madison POMS. This was complicated by the

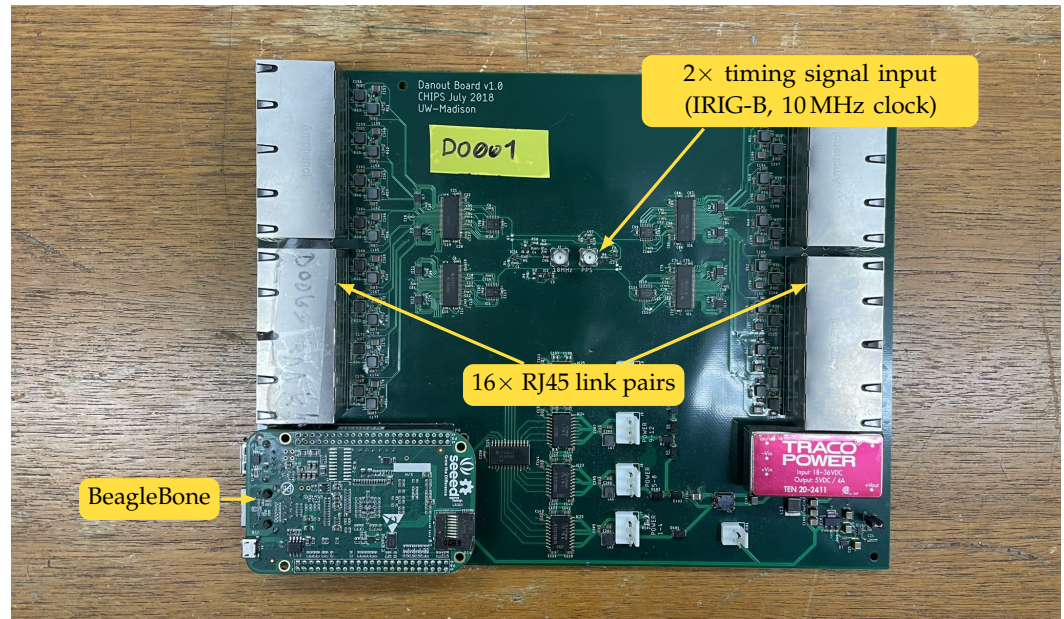


Figure 16. Danout board with BeagleBone® Green SBC. Upstream and downstream ports are annotated.

fact that unlike CLBs, Badger boards were not directly compatible with the WR standard. Madison fanouts therefore had to convert time from the WR network to electrical timing signals, which were transmitted to POMs alongside data traffic. This was the purpose of a PCB called Danout board, which is shown in Figure 16. Danout board accepted 100 Mbit Ethernet links from upstream as well as a pair of timing signals, which it injected into a corresponding number of downstream links towards Badger boards. Since these connections also carried power, the Danout board was able to remotely switch individual POMs on or off through I²C-controlled relays. The Danout board was supervised by a BeagleBone SBC, which was interfaced with the PCB by the same header mechanism used in Badger boards.

Besides the Danout board, Madison fanouts included conventional Ethernet switches. These network elements multiplexed 16 lines of upstream data traffic into a single metallic Ethernet line, which was routed through a device called *WR Lite Embedded Node* (WR-LEN, shown in Figure 17) [24]. As its name suggests, WR-LEN was a WR node programmed to act as a slave in the WR network, which allowed it to receive precise time from higher levels of the DAQ system. WR-LEN acted as a media converter and adapted metallic Ethernet to a fibre optic link compliant with the WR standard. In addition, WR-LEN converted time from WR network to IRIG-B and 10 MHz clock signals, which were immediately consumed by the Danout board. Just like Nikhef fanouts, the upstream fibre from WR-LEN was patched to shore infrastructure through the junction box.

The junction box was the main hub for the entire submerged detector, which was responsible for distributing communications and power from the umbilical towards fanouts. To switch fanout power, the junction box carried two relay boards that were controlled remotely over the network, much like relays installed in Nikhef fanouts. For increased resilience against electrical faults, downstream power lines were protected by trip gates that automatically interrupted them if current surges were detected. In the event of flooding, this safety measure allowed the unaffected part of the detector to remain isolated from damaged subsystems.

WR network from fanouts was transmitted through the umbilical by coarse wavelength division multiplexing (CWDM). This method encoded traffic from 16 single-mode fibres into a single armoured multi-mode fibre that carried light of 32 distinct wavelengths



(a) Front panel.

(b) Back panel.

Figure 17. Commercially available WR-LEN. The front panel shows timing signal outputs (circular SMA ports on the left) and SFP receptacles (rectangular ports in the middle) for bidirectional connection to a WR network. The back panel has power connector (left) and a single RJ45 port (right) for 1 Gbit Ethernet link.

along the umbilical. This removed the need for any Layer 2 switching inside the junction box. Instead, all WR switches and WR-LENs from fanouts interacted transparently with the network elements on the shore.

Since the junction box presented a single point of failure, extensive testing was performed prior to its installation in CHIPS-5. The largest hazard was seen to be flooding due to a pressure seal fault. The design of the container mitigated this by employing feedthroughs and water-resistant bulkheads near all interfaces and openings, just like other electronics containers. To minimize probability of accidental failure following deployment, the junction box underwent dedicated pressure tests. In addition, all infrastructure electronics were jointly and independently tested prior to their installation in containers and waterproofing. Figure 18 shows one of these tests, providing an adequate overview of DAQ infrastructure deployed underwater.

3.3. Shore facilities

Power lines and the multi-mode fibre that emerged from the umbilical were routed into an electronics hut, which was situated on the shore of the mining pit alongside the water treatment hut. This small building housed remaining DAQ infrastructure that connected the deployed detector to power mains, remotely controlled its instrumentation and transmitted its measurements to Fermilab through the Internet. This equipment is shown in Figure 19.

At the root of the WR network was a pair of linked WR switches, which consumed optical fibres from the umbilical through a CWDM multiplexer. Contrary to intuition, these root WR switches were not equivalent. One of them consumed timing signals from a GNSS receiver, and therefore occupied the role of the grandmaster node in the time distribution hierarchy. In contrast, the other switch merely expanded the breadth of the network at the highest level. This way, WR switches inside Nikhef fanouts and WR-LENs inside Madison fanouts were always at most 2 hops away from the grandmaster.

To ensure that the WR network was reachable from non-WR elements installed upstream, root WR switches were patched into a conventional 10 Gbit Ethernet switch. Since this switch was incompatible with WR, this divided the DAQ network into two bridged segments: a WR segment that included both root WR switches as well as all electronics beyond the umbilical, and a conventional Ethernet segment that contained peripherals dedicated to detector control and data handling. The most prominent of these devices were 4 computers that hosted DAQ software, which is further described in Section 4. These computers primarily exchanged data and control messages with detector instrumentation, and were therefore adequately equipped to process incoming data in real-time with re-

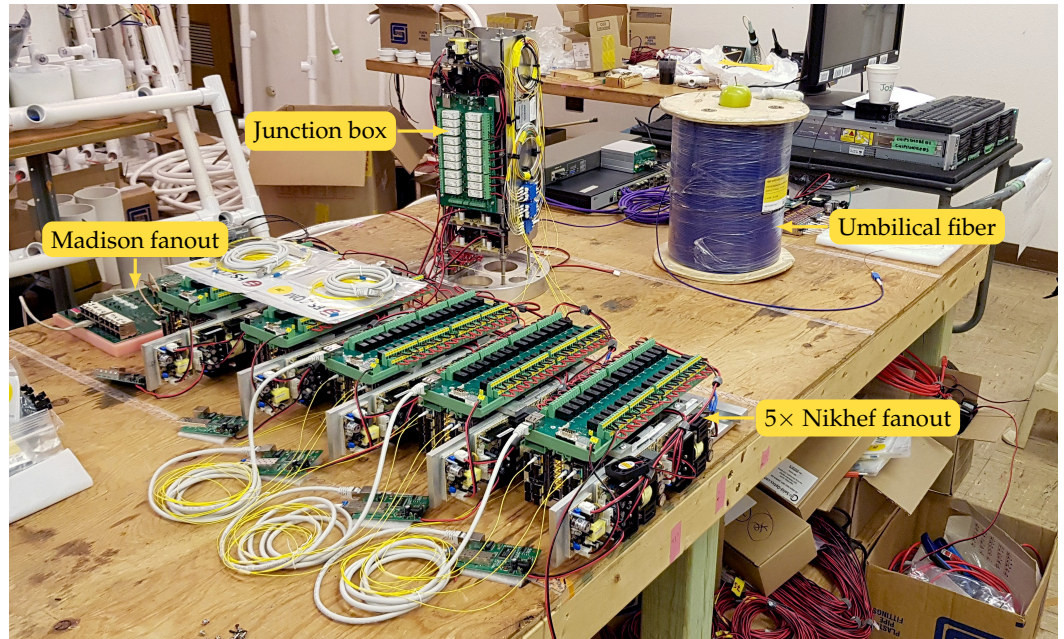


Figure 18. Infrastructure electronics before their installation into fanout containers and the junction box. Shore hut equipment is visible in the far right. Background photograph courtesy of J. Tingey.

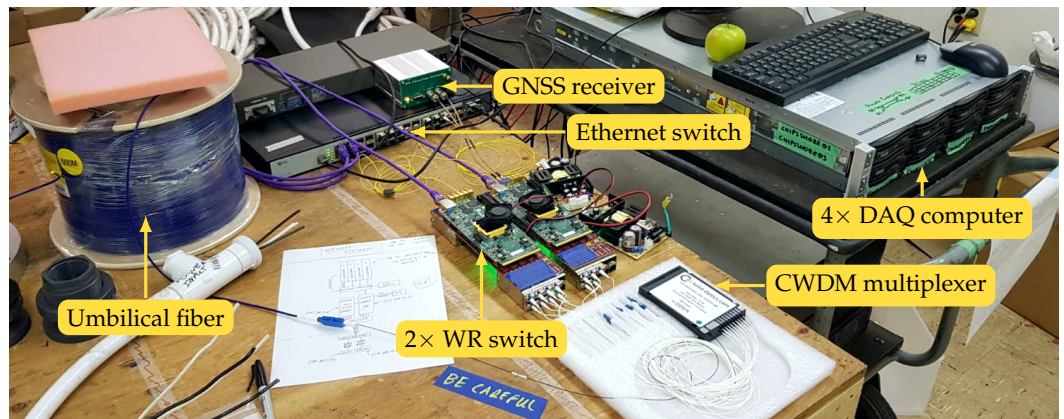


Figure 19. DAQ infrastructure before installation in the electronics hut. Background photograph courtesy of J. Tingey.

dundant capacity. In addition, they included sufficient persistent storage to hold logs and measurements for a period of at least several weeks.

The DAQ network was connected upstream to the Internet through pre-existing infrastructure managed by the PolyMet Mining Corporation. This permitted remote access for DAQ operators, hardware monitoring and alerting, data transfers towards Fermilab and low-latency delivery of NuMI spill triggers through CHIPS-5 TDS. External access to the DAQ network was facilitated by encrypted virtual private network (VPN) over Layer 2 Tunnelling Protocol (L2TP).

Besides computers and network infrastructure, the electronics hut also housed a cooling unit and power distribution systems, which supplied mains voltage to both shore huts as well as the deployed detector. While majority of devices were connected to an unprotected power line, which was potentially susceptible to outages, computers and key network elements drew power through an uninterruptible power supply (UPS). In the event of a power outage this provided at least 15 min of battery capacity, which was sufficient for a graceful shutdown of any ongoing DAQ operations. A comprehensive overview of DAQ hardware used by CHIPS-5 is shown in Figure 20.

4. Software

After traversing the topology of DAQ hardware described in the previous section, measurements from PMTs converged at 4 computers situated inside the electronics hut. These computers, labelled *Shore DAQ 1-4*, hosted purpose-built software that constituted the next stage of the DAQ system. While it was desirable to deploy majority of programs to these machines given their relatively close proximity to the detector, it is worth noting that various components relevant to DAQ also operated in other locations. Firstly, CLBs and MicroDAQs inside the detector were programmed with dedicated firmware, which is beyond the scope of this work [25,26]. Secondly, Fermilab provided a persistent storage facility for acquired data, which was planned to be used for physics analysis in later stages of the project. A DAQ subsystem was responsible for periodic data transfers from shore machines to this database. And finally, Fermilab infrastructure also hosted parts of CHIPS-5 Timing Distribution System (TDS), which is discussed in other literature [27].

Following conventional DAQ paradigm, the shore computers were programmed to perform three basic tasks:

1. Monitor the state of the detector.
2. Control auxiliary electronics and detector instrumentation.
3. Receive, process and store data from PMTs.

These tasks were implemented by a suite of single-purpose C++ programs [28], which were designed to function together in concert, much like detector hardware. This architecture choice had several advantages. Since each program had a clearly defined role and purpose, source code was relatively simple to write, and easy to inspect and verify. Furthermore, compartmentalization allowed DAQ programs to be individually instrumented for monitoring and independently reset upon crashing. Fault tolerance was further promoted by running software on only 2 out of 4 shore computers at any one time, leaving the other pair available as backups in case of failure or service interventions. To protect systems from hard drive faults, all persistent local storage was consolidated in a redundant array of inexpensive disks (RAID) [29].

Shore computers were provisioned with Community Enterprise Operating System (CentOS) Linux 7 [30], which was the successor of Scientific Linux 6. To minimize system overhead, DAQ programs were deployed on 'bare metal' without virtualization and executed continuously as daemons (background processes). This allowed software to be supervised within the `systemd` service manager [31], which was responsible for state tracking and automatic recovery from failures or degenerate states.

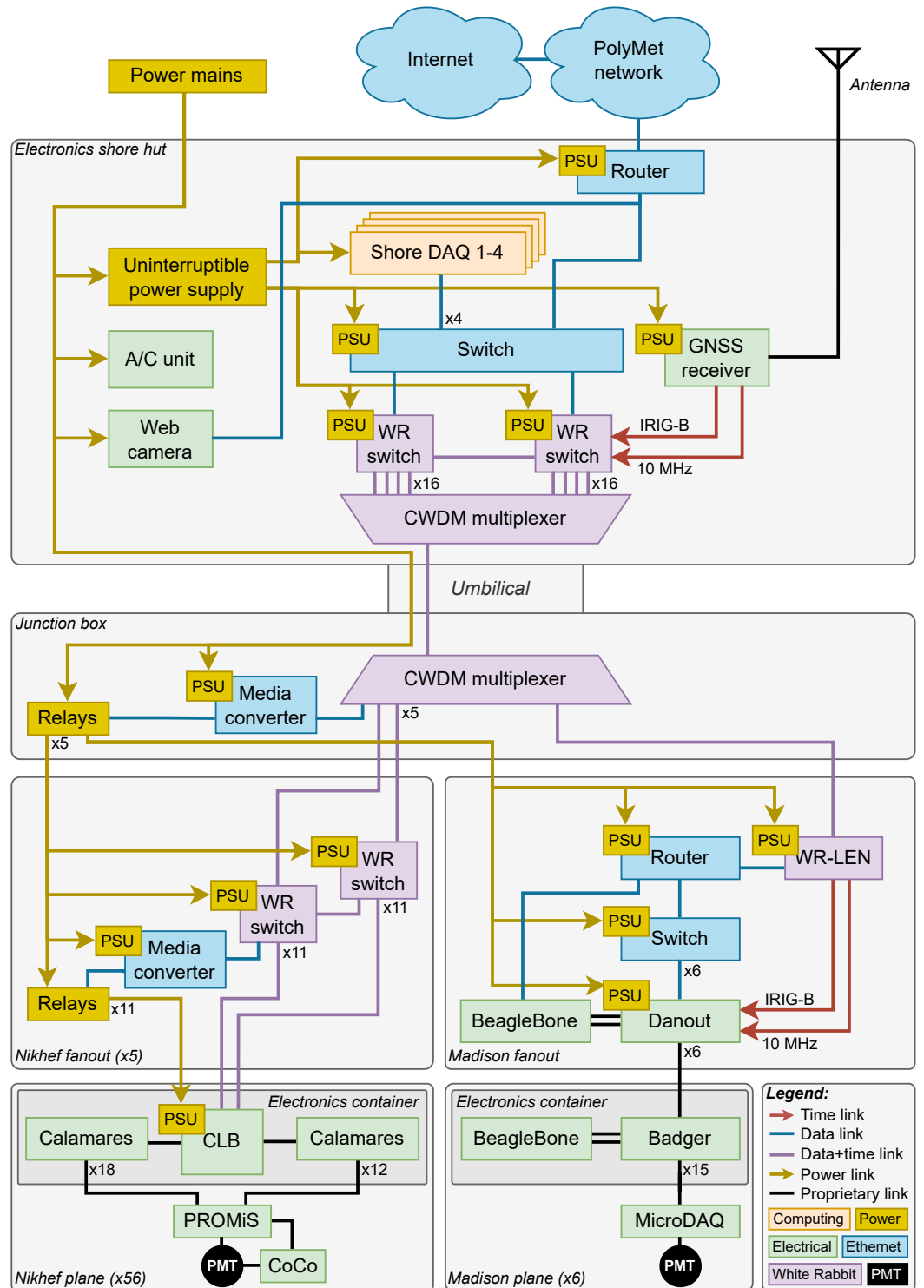


Figure 20. Diagram of DAQ hardware, showing organization of instrumentation inside CHIPS-5 and on the shore. While measured data generally flow from the bottom up, commands, timing signals and power flows down from the top.

4.1. Monitoring

To correctly control the detector following its deployment, it was important for DAQ operators to have complete and accurate representation of its state in real-time. This motivated development of a *monitoring system*, which collected, visualized and archived various key indicators of interest over time. In addition, this system also dispatched urgent alerts whenever observed quantities exceeded specified tolerances or anomalies occurred with respect to established baseline.

The monitoring system used in CHIPS-5 was based on Elasticsearch [32], which is an open-source document-based database system with broad applications in the field of infrastructure monitoring. This product was ideally suited for the task since its distributed architecture efficiently enabled periodic and simultaneous collection of structured time-ordered data from a wide range of sources. Based on desired use cases, Elasticsearch permits users to define indices that determine internal data organization strategy for fast retrieval, which is facilitated through Elasticsearch Query Language (ESQL). In addition, Elasticsearch is accompanied by a diverse set of tools and integrations, collectively known as the Elastic Stack (or ELK Stack) [33], which readily implement compatibility with frequently used data sources and visualization methods.

For CHIPS-5, the Elasticsearch database engine was hosted from a single shore computer. Even though its underlying technology supported distributed operation over multiple machines, expected data throughput was sufficiently low to justify this simpler, more compact installation. Under normal operation the software exposed an application programming interface (API) on the DAQ network, which received new information from data sources throughout the detector, as well as visualization requests and ESQL queries from operators.

Data committed to the monitoring system came from several groups of sources. Firstly, the most basic information came from periodic health checks, which were directed from a Heartbeat process to all devices connected to the DAQ network. A single such check probed roundtrip latency of a conventional Internet Control Message Protocol (ICMP) Echo Request/Reply exchange. In addition, all Linux computers (shore machines and BeagleBones) ran additional Metricbeat processes, which collected system logs, recorded state of all managed services (including DAQ programs) and sampled hardware counters. Similarly, compatible network elements (routers, switches and WR switches) were configured to export their state to Elasticsearch over Simple Network Management Protocol (SNMP).

Secondly, all CHIPS DAQ programs were instrumented to collect and publish their performance indicators through Elasticsearch API. This information included detailed condition of all detector planes, local meteorological data (temperature, atmospheric pressure and relative humidity), the state of the GNSS time source, number of hits registered from individual PMTs, TDS metrics, and NuMI operations data scraped from Fermilab Accelerator Division (AD) website.

Finally, Elasticsearch consumed hit monitoring messages generated by software running on-board CLBs and BeagleBones. These packets served as an independent integrity check throughout runs, and therefore needed to be archived for quality control purposes. Their significance is fully explained in Section 4.3.

Information accumulated by the CHIPS-5 monitoring system was presented to operators through the Kibana frontend [34]. In addition to issuing ESQL queries and visualizing their outputs, this versatile web application was programmed with a collection of dashboards that topically compiled plots relevant to frequently performed DAQ operations. One such dashboard is shown in Figure 21. Kibana also included rule-based alerting mechanism, which was directed at Slack channels and email addresses of DAQ operators.

4.2. Detector control

With accurate information supplied by the monitoring system, DAQ operators were able to inspect the state of individual components of the detector, and determine future

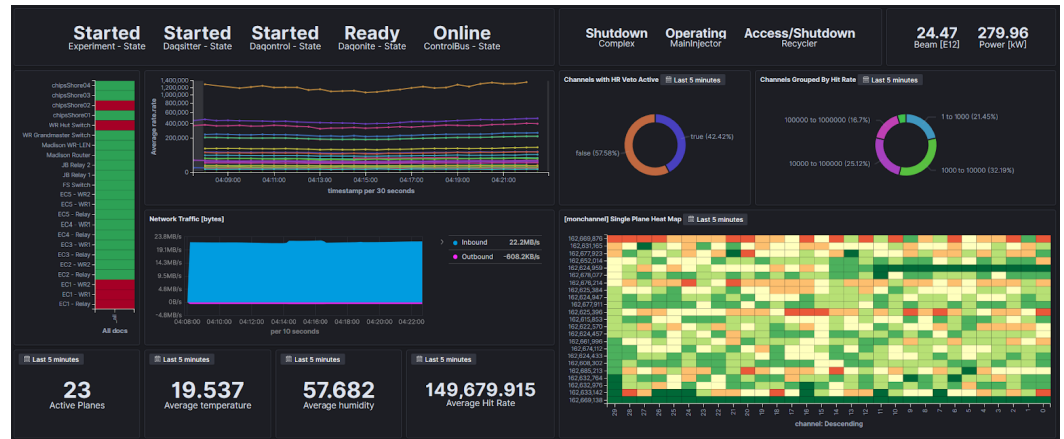


Figure 21. Monitoring dashboard visualized by Kibana, showing PMT hit rates as well as state of the FSM and the NuMI beam reported from Fermilab. Plots and gauges are fed by data retrieved from Elasticsearch through ESQL queries. Screenshot courtesy of J. Tingey.

actions. Expedient and reliable implementation of their decisions was the purpose of the *detector control system*.

Since the number of controllable elements in the first phase of CHIPS-5 deployment was on the order of hundreds with planned future upgrades reaching thousands, it was viewed as intractable to control each component individually. This motivated division of the control system into three subsystems: a hardware control system (HCS) that interacted with detector hardware, a finite state machine (FSM) that tracked dependencies and orchestrated equipment, and a control bus that facilitated communications. DAQ operators typically issued high-level commands to FSM, which in turn generated more concrete instructions to HCS that carried them out. Messages exchanged between operators, FSM and HCS were dispatched through the control bus.

Representing the lower stage of the control system, HCS directly interacted with a diverse set of components, such as CLBs, BeagleBones and electrical relays. To this end, it implemented device-specific control protocols that exposed APIs of parametrized actions and acknowledgements. Included among these were probing operations, which were regularly executed during health checks and forwarded to Elasticsearch, providing a source of monitoring information. Control exchanges with hardware were transmitted through DAQ network over Transmission Control Protocol (TCP). To prevent network congestion from disrupting these communications, fixed minimal bandwidth for control data frames was allocated in network infrastructure. In addition, controlled equipment was isolated in multiple virtual local area networks (VLANs).

It is worth noting that due to distinctiveness of instrumentation carried by Nikhef and Madison planes, their components responded to different low-level instructions that often performed similar actions. To prevent unnecessarily increased complexity in higher stages of the control system, HCS acted as a hardware abstraction layer and presented a unified control interface for all planes towards FSM. This is illustrated in Figure 22. Implementation of control protocols was consolidated in a *DAQ-control* service, which was hosted at one of the shore computers; by convention the same instance that handled monitoring.

Higher up in the control system, FSM implemented finite-state automata that tracked the CHIPS-5 detector and all of its components. This method was selected because of its formal verifiability through model checking, high reliability and wide adoption in commercial industrial applications, which typically employ supervisory control and data acquisition (SCADA) systems for the same task. FSM for CHIPS-5 was built around the open-source TinyFSM package [35]. It closely modelled detector hardware as a tree graph, where nodes represented individual components and directed edges connected nodes with a dependency relationship. In this graph, each node was characterized by a discrete state that described its configuration, health and readiness for DAQ operations. The set of all

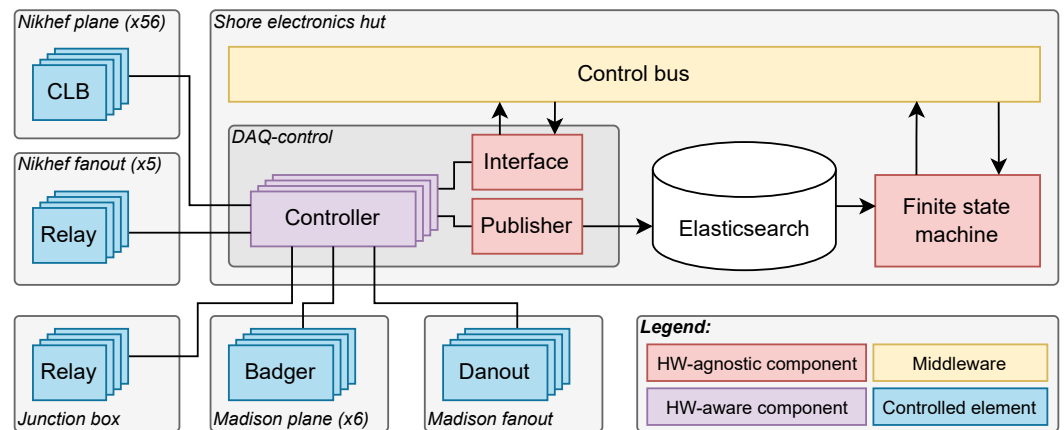


Figure 22. Diagram showing interaction of monitoring and control systems with controlled elements of CHIPS-5. Separation between hardware-aware (violet) and hardware-agnostic (red) components is indicated by color.

possible states was identical across all nodes, which allowed states to propagate upward along the topology of the graph according to a simple rule: if all children of a node shared the same state, the node attained that state. Conversely, if a node had children in multiple different states, it was marked as inconsistent, which usually attracted operator attention. The state of the entire detector was understood to be the state of the root of the tree.

To accurately determine the state of each node, FSM continuously consumed information from the monitoring system. Based on that, DAQ operators were presented with a range of available actions that would initiate transitions to other reachable states. Each such action was applicable to individual nodes as well as larger subtrees of the graph. Once a state transition was requested, FSM generated messages to all affected nodes through the control bus, which incorporated low-level instructions to HCS that typically rendered nodes inconsistent for a short period of time. Once HCS registered command acknowledgments, information retrieved through the monitoring system permitted FSM to complete the state transition, eventually reaching a consistent state. A similar process occurred when failures were detected, with the notable distinction of the target state.

Figure 23 shows a diagram of FSM states relevant to DAQ operations. From the initial state, detector components underwent a batch configuration procedure, which applied calibrated cable delays, high voltages and digitization thresholds to individual PMTs. In addition, it programmed measurement parameters and directed data flow at desired sinks. Successful configuration transitioned the detector to the ‘configured’ state, primed to begin measurement. To begin registering PMT hits, the operator moved to the ‘data flowing’ state, which started ingest workers on the receiving side and opened shutter in CLBs and BeagleBones. At that point, the detector became sensitive and DAQ network started experiencing increased traffic. This sometimes included short-lived surges (empirically, up to 5.66 Gbit/s), particularly when detector volume had been recently exposed to light. After a brief delay, which allowed data rates to stabilize, the operator commanded FSM to transition to the ‘run’ state that signalled ingest workers to enable data processing and collection. When this state was reached, measurements started accumulating as data files in persistent storage. To return the detector back to insensitive state, where its configuration could be adjusted, operators followed a reversed sequence of state transitions.

The communication channel that facilitated command input to FSM and connected FSM to HCS, was a brokerless control bus based on the NNG middleware [36]. This open-source package was selected because of its minimalist, lightweight implementation and focus on increased robustness in production environments. Datagrams dispatched through the control bus were transmitted as reliable broadcasts through UNIX domain sockets, where all bus participants acknowledged message reception.

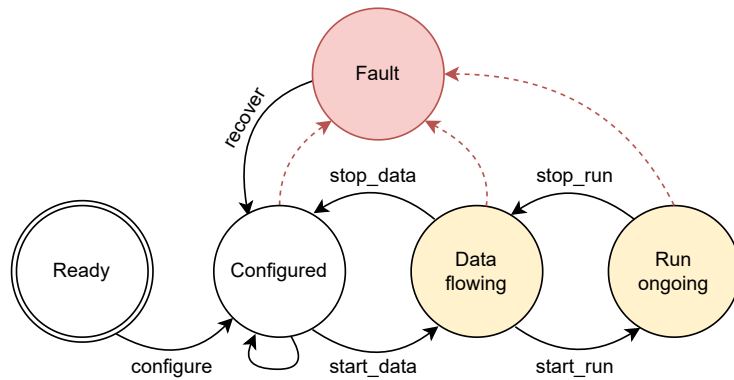


Figure 23. Simplified state diagram of the CHIPS-5 FSM. The initial state is marked with a double border, whereas states where measurements flow through DAQ infrastructure are highlighted in yellow. Solid black and dashed red arrows indicate successful and failed state transitions, respectively.

4.3. Data ingest

When data flowed through DAQ network during runs, streams of information generated by planes were directed at multiple sinks, collectively known as *data ingest*. Unlike monitoring and control systems, which aimed to provide low latency and high reliability, data ingest focused on efficient handling of large data volumes with a degree of tolerance for data loss.

It is worth noting that high throughput was a direct consequence of the design decision to use self-triggering in PROMiS and MicroDAQ. At a later point in the project, TDS delivered the capability to trigger MicroDAQs externally by accelerator spills, which in part alleviated this effect. Nevertheless, this upgrade achieved only a modest reduction of overall data rates due to disproportionately small fraction of Madison planes in the detector. For that reason, efficiency under high data rates remained a priority even with external triggering.

At the level of CLBs and BeagleBones, PMT hits were aggregated into packets called *optical data*. Representing the primary data output of a single plane, these messages were at most 8.8 kB large², and carried compressed ToA, ToT and channel address for every hit. Optical data were transmitted over User Datagram Protocol (UDP), which is susceptible to data loss under certain conditions. To detect and track this undesirable effect throughout runs, CLBs and BeagleBones generated a secondary data output, known as *monitoring data* (not to be confused with data gathered by the CHIPS-5 monitoring system). Monitoring packets were emitted every 10 ms and contained metadata accompanied by snapshots of hit counters, as seen by the sender. By keeping independent hit counters and regularly comparing their values with these snapshots, the receiver was able to detect and quantify the fraction of dropped optical datagrams.

Under normal operation, packets from planes converged at 2 out of 4 shore machines. To fully utilize available processing capacity, a single machine was dedicated to each type of data, leaving the other pair as backups. Monitoring packets were received by the *DAQ-monitor* service, which decoded and forwarded hit counts to the monitoring system. This provided operators as well as hit handling software with a near real-time integrity check. In concert, optical data was directed at the *DAQ-onite*³ service, which was responsible for producing measurement files compatible with the ROOT analysis framework [37].

Since both ingest services were designed to process data rates on the order of 10 Gbit/s, their C++ implementation utilized multi-threading and asynchronous input/output (ASIO)

² This was defined by setting Ethernet maximum transmission unit (MTU) to 9000 B, in contrast to conventional 1500 B, for so-called jumbo data frames.

³ The name ‘DAQ-onite’ was inspired by taconite, which is a type of iron ore mined in the region surrounding the CHIPS-5 detector site.

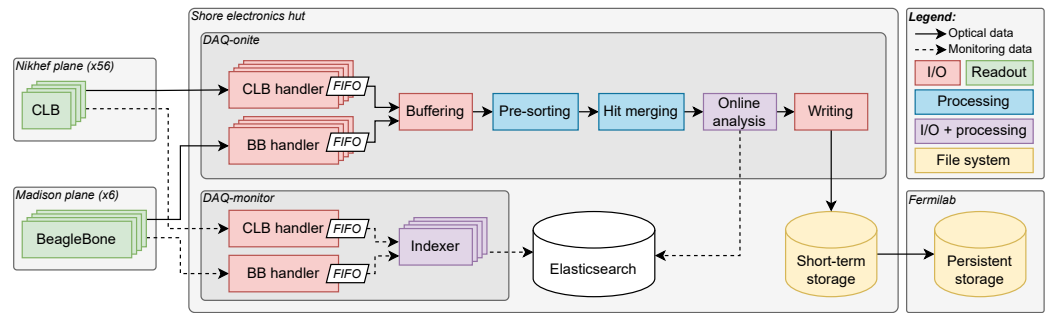


Figure 24. Diagram showing flow of optical and monitoring data from planes to ingest services and storage facilities. Here ‘FIFO’ abbreviates *first in, first out*, which is a lockless data structure utilized to relay data between processing threads.

operations, which aim to avoid program suspension (known as *blocking*) during time-consuming data access. For this reason, both programs interacted with network sockets and files through Boost.Asio [38]. This open-source package was selected because of its focus on high throughput, well-characterized performance and abundance of adjustable parameters that permitted tunable scaling given specific computing hardware.

The internal architecture of an ingest service was divided into a hardware-oriented frontend, which consisted of packet handlers for Nikhef and Madison planes, and application-specific backend. This is illustrated in Figure 24. To minimize overhead, multiple parallel instances of frontend handlers were hosted in a thread pool that constituted a Boost I/O service. Each handler consumed UDP datagrams, decoded them and pushed their contents into a lockless memory data structure, which was continuously evacuated by the backend on another thread. In the case of DAQ-onite, the backend was a data handler that consolidated PMT hits from planes, performed online analysis and saved outputs to ROOT files. This was later upgraded to associate hit ToA with incoming spill triggers, delivered by TDS from Fermilab accelerator complex [27]. In DAQ-monitor, the backend was an indexer that adapted and transmitted hit counts to Elasticsearch as structured documents.

4.4. Hit merging and event building

To complement immediate feedback from monitoring packets, DAQ-onite provided operators with data quality indicators through the monitoring system. Since these quantities often probed properties of individual events (coincident groups of hits), the program needed to ensure that hits arriving in parallel were first correctly interleaved into a single sequence, which was monotonically ordered by hit ToA. This was the purpose of the *hit merging* stage that operated in real-time during runs.

The algorithm used to interleave hits was based on a conventional k -way merge strategy [39], which was previously used with success in the KM3NeT project. This method modelled k input hit sequences as leaves of a binary tree. The algorithm independently processed leaf pairs in passes that linearly enumerated both corresponding sequences and took hits from one or the other based on the lowest available ToA. In result, each leaf pair in the tree gave rise to a new parent node, which corresponded to a sequence containing hits from both children. This way, the merging process repeated multiple times, halving the number of nodes at the topmost level in every iteration. After at most $\mathcal{O}(\log_2 k)$ steps, all input sequences were merged into a single root node that contained output of the algorithm. This is illustrated in Figure 25.

Even though the k -way merge algorithm was formally correct, it made several ambitious assumptions that needed to be examined before its practical application in CHIPS-5. For instance, the algorithm expected input hit sequences to be finite arrays of known size, whereas in reality hits were registered continuously over time. Given the scale of the detector and hardware constraints of DAQ computers, it was intractable to retain optical data in memory until the end of a run, and only merge afterwards. For that reason, inputs

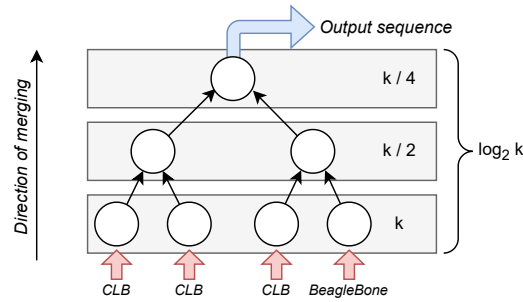
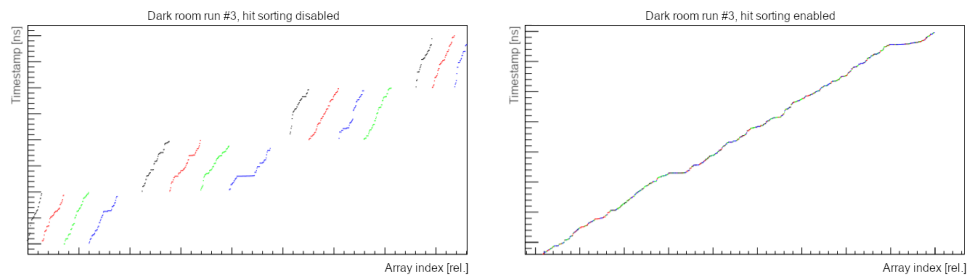


Figure 25. Iterative merging of k hit sequences. Input sequences (red) are consolidated from the bottom of the binary tree upward, along the direction indicated by arrows. The output sequence (blue) is obtained from the root of the tree.



(a) Received optical data from a CLB.

(b) Pre-sorted batch, ready for hit merging.

Figure 26. Localized disorder found in CLB optical data during a dark room measurement. Plots show hit ToA as a function of hit number before (a) and after (b) the pre-sorting stage. PMT channels are coded by point color.

were buffered in batches of fixed size. Depending on hit rates, DAQ-onite typically filled a single batch within seconds. This allowed the merging algorithm to always work with fixed-size inputs. In later stages of the project, hit merging was upgraded to process batches simultaneously on multiple threads in parallel to further increase performance.

Another assumption made by the algorithm was that input hit sequences were independently well-ordered before they entered the merging stage. If this assumption held, a pair of sequences could be merged efficiently by a single linear pass. Sadly, even though CLB optical data was mostly ordered overall, hit stream analysis revealed localized regions of disorder shown in Figure 26a. Since these regions aligned with channel boundaries, it is possible to speculate that CLB firmware internally switched between channels in a round-robin scheme. While hits were correctly ordered within the scope of each channel, no effort was made to interleave hits between channels.

To address this hit disorder in DAQ-onite, additional pre-sorting stage was introduced between buffering and hit merging. In the course of pre-sorting, all k input hit sequences were independently processed with insertion sort [40]. Even though this algorithm is considered suboptimal for general use cases due to worst-case complexity of $\mathcal{O}(n^2)$ given n hits, its application here was well-motivated. Since complexity of insertion sort is proportional to the degree of disorder of its input, applying it to a nearly ordered hit sequence typically consumed only negligible fraction of computing resources. In an ideal case, where the input was already perfectly ordered, complexity of the algorithm was reduced to appreciable $\mathcal{O}(n)$. In addition, the use of insertion sort in pre-sorting also brought practical benefits for Madison planes. Even though Field Hub App internally interleaved hits from MicroDAQs before transmission, high hit rates sometimes tested limits of BeagleBone processing capacity. In such situations, the existence of pre-sorting allowed compute loads to be alleviated by seamlessly transferring them upstream to DAQ-onite without jeopardizing correctness of collected data.

Moving past the merging stage, hits were clustered into events by comparing differences of successive ToA, and grouping hits that fell into an adjustable time window on the order of nanoseconds. This was also the point where events were classified as cosmic if they contained any hits from veto PMTs, and where data quality indicators were calculated. Following that, data were committed to persistent storage in the ROOT file format.

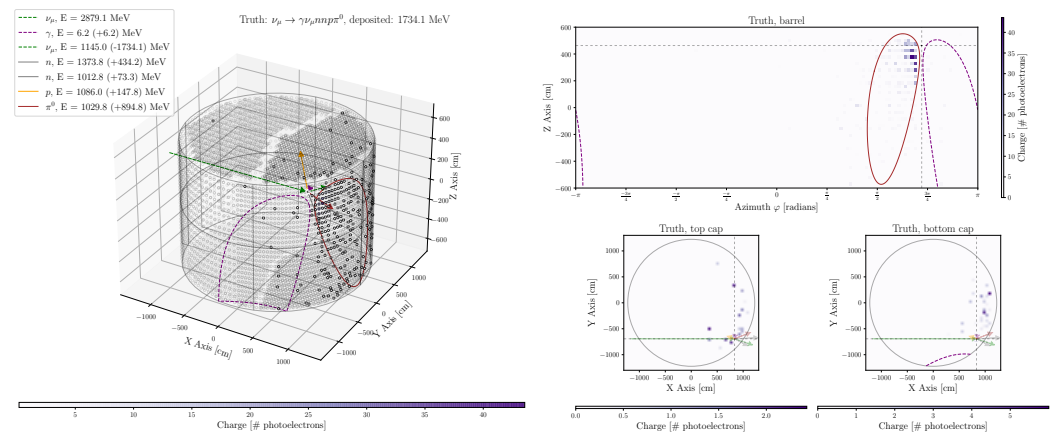
4.5. Offline analysis

Produced measurement files were temporarily retained at shore computers. Due to their relatively low size, locally available storage capacity sufficed for several weeks of continuous acquisition, if necessary. Under normal operation, however, data were regularly transferred over the Internet to a permanent storage facility at Fermilab. From there, archived measurements were subject to *offline analysis*, which was planned to be implemented in batch computing jobs submitted to Open Science Grid [41]. Consistently with design principles of the CHIPS project, offline analysis explored novel approaches to neutrino event simulation, reconstruction and classification, which had potential to reduce complexity and computing loads while maintaining or possibly improving accuracy.

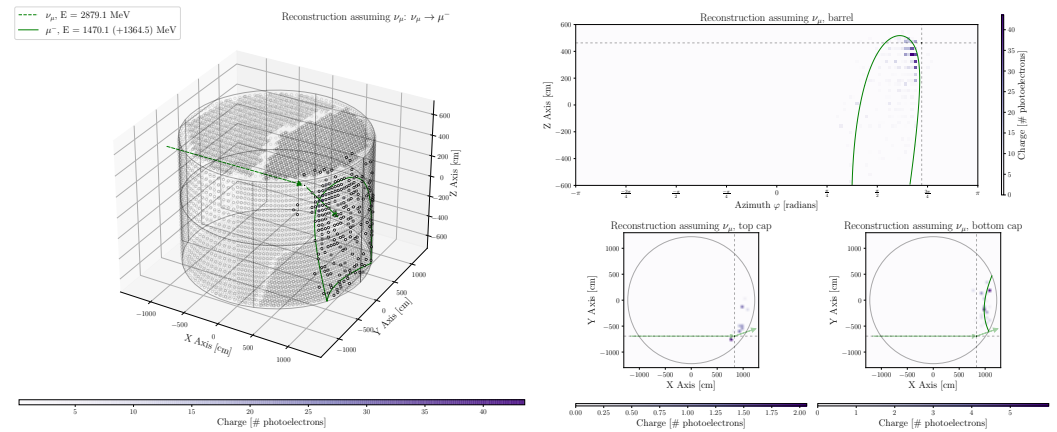
A comprehensive description of a likelihood-based event reconstruction algorithm is available in reference [42]. This method required prior generation of a sizeable data sample using the WCSim package [43], which was adapted for CHIPS geometry from its original application in $\bar{\nu}_k$ and LBNE. In its implementation [44,45], beam and cosmic events, supplied by the GENIE [46] and CRY [47] generators respectively, produced digitized PMT response that was simulated using the GEANT4 toolkit [48]. When presented with a real-world event, the reconstruction algorithm began by identifying Cherenkov rings in a geometric hit map using circular Hough transform [49]. In subsequent iterations, seeded tracks were fitted by maximizing likelihood of observed hits given previously simulated detector behaviour. A result of such a fit is shown in Figure 27. The final stage of the algorithm employed two feed-forward artificial neural networks (ANNs) for particle identification (PID). At input, these networks accepted vectors of various manually selected features, such as hit count ratios yielded by the preceding stage. At output, the networks produced a classification that labelled events as electron-like, muon-like or NC interactions.

While likelihood-driven optimization presented a viable method of event reconstruction, its implementation was inherently based on empirical observations and hand-engineered features that provided no guarantee of optimality. This motivated development of alternative methodology, which at its core employed convolutional neural networks (CNNs). Since these models perform parametrized feature extraction in initial layers of their network architecture, their training was expected to overcome the optimality issue by favouring features best-suited to the task.

Event reconstruction techniques based on CNNs are discussed in reference [50]. In many aspects, these methods built on their likelihood-based counterparts by adapting their simulation software for production of training datasets. Simulated events were arranged into geometric hit maps that directly encoded digitized ToT and ToA, complemented by an additional parameter map that was calculated by Hough transform. These two-dimensional maps were interpreted as images and fed into a deep network known as *chipsnet*, which was largely based on the widely adopted VGG architecture [51]. This gave rise to three categories of networks, distinguished by interpretation of their output layer: the *cosmic rejection network* that classified event origin as beam or cosmic, the *beam classification network* that further tagged beam events as electron-like, muon-like or NC interactions, and the *neutrino energy network* that performed regression of neutrino energies. In evaluation, these models were shown to yield appreciable improvements over likelihood-based fitting. This can be for example demonstrated in terms of errors in neutrino energy reconstruction, which are compared in Figure 28.



(a) Visualization of the simulated ground truth.



(b) Most probable hypothesis found by a likelihood-based fit.

Figure 27. Example of likelihood-based fitting. Plots display a simulated ν_μ interaction (a) and its reconstruction (b), visualized as charge collected by PMTs (color axis) and Cherenkov cone sections (contours). While the left view shows a perspective of the detector geometry, two-dimensional maps on the right correspond to inner faces of the detector. Particle trajectories are indicated by arrows, the interaction vertex is marked by a star.

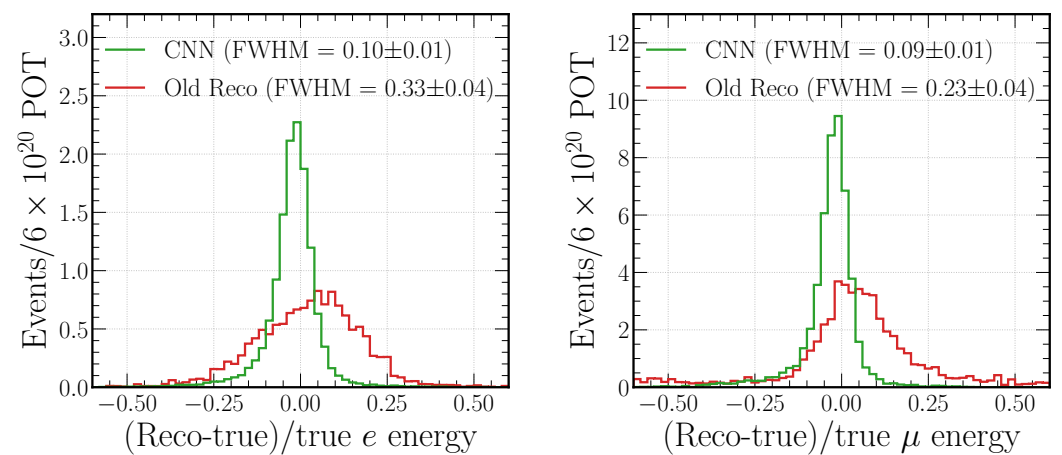


Figure 28. Comparison of neutrino energy reconstruction accuracy by likelihood-based fitting (red) and a CNN (green). Plots show the difference between reconstructed and true energies of quasi-elastic CC ν_e (left) and ν_μ (right) interactions on a sample of 400×10^3 beam events. The result was taken from reference [50].

5. Conclusion

The goal of the CHIPS project was to show that affordable neutrino detector technology could be implemented using commercially available components, rather than their more expensive purpose-built counterparts. The explored domain of cost reduction strategies included novel design concepts, construction methods and DAQ technology. To this end, modern instrumentation was developed for use in the recent CHIPS-5 detector prototype, which was based on two distinctive but functionally equivalent sets of hardware. Inspired by the architecture of CHIPS-5 itself, this DAQ system adopted a modular approach that allows a basic detector to be composed from a small number of interconnected POMs, which can be easily serviced and readily scaled up. In spite of its versatility, the presented technology does not make undesirable compromises on data quality. Specifically, its sub-nanosecond time resolution is sufficient to reconstruct directional sources of Cherenkov light within detector volume. Furthermore, its compatibility with standardized timing distribution systems permits synchronization and interoperability with other similar detectors.

Hardware components of the presented DAQ solution are accompanied by a suite of high-performance programs that are capable of monitoring, controlling and reading out instruments over a conventional Ethernet network. This software was designed with a robust and parallel architecture, which allows it to be efficiently deployed in distributed computing facilities in order to orchestrate detectors on the scale of CHIPS-5. In addition to decoding and saving received data, the software is able to recognize coincident events in real-time and associate this information with triggers generated by neutrino spills. Offline event reconstruction is facilitated by two alternative algorithms: a conventional likelihood-based fit and a more modern method that delegates feature extraction as well as event classification to a CNN. Both of these techniques have shown acceptable accuracy when evaluated with simulated events.

Even though the CHIPS-5 prototype was ultimately unable to observe NuMI neutrinos due to deployment issues, its development revealed potential for appreciable cost reductions achieved by transition to standardized mass-produced components and modular architecture. Furthermore, during the course of the project the presented DAQ system successfully passed a number of commissioning tests, indicating that the instrumentation was functional and suitable for scientific use at the intended scale. The technology is currently reused in other ongoing experiments.

6. Acknowledgements

This work was supported by Fermilab; the Leverhulme Trust Research Project Grant; U.S. Department of Energy; and the European Research Council funding for the CHROMIUM project. Fermilab is operated by Fermi Research Alliance, LLC, under Contract No. DE-AC02-07CH11359 with the U.S. DOE.

The CHIPS collaboration would like to thank the Wisconsin IceCube Particle Astrophysics Center, University of Wisconsin–Madison, University College London, University of Alberta, University of Minnesota Duluth and Aix-Marseille University. Finally, the CHIPS collaboration would like to thank PolyMet and Cleveland-Cliffs for hosting the experiment.

References

1. Adamson, P.; Austin, J.; Cao, S.V.; Coelho, J.A.B.; Davies, G.S.; Evans, J.J.; Guzowski, P.; Habig, A.; Holin, A.; Huang, J.; et al. Cherenkov Detectors In Mine PitS (CHIPS) Letter of Intent to FNAL. Technical report, Fermi National Accelerator Laboratory, Batavia, IL (United States), 2013. <https://doi.org/10.2172/1342789>.
2. Rancurel, B.A.; Angelides, N.; Augustoni, G.; Bash, S.; Bergmann, B.; Bertschinger, N.; Bizouard, P.; Campbell, M.; Cao, S.; Carroll, T.; et al. The Design and Construction of the CHIPS Water Cherenkov Neutrino Detector. *arXiv preprint arXiv:2401.11728* **2024**.
3. Adamson, P.; Anderson, K.; Andrews, M.; Andrews, R.; Anghel, I.; Augustine, D.; Aurisano, A.; Avvakumov, S.; Ayres, D.; Baller, B.; et al. The NuMI neutrino beam. *Nuclear Instruments and Methods in Physics Research Section A: Accelerators, Spectrometers, Detectors and Associated Equipment* **2016**, *806*, 279–306.
4. Hainan Zhanchuang Photonics. *Photomultiplier Tubes*, 2019. <http://www.hzcp Photonics.com/products/ProductManual.pdf>.

5. Arnold, R.; Augier, C.; Bakalyarov, A.; Baker, J.; Barabash, A.; Bernaudin, P.; Bouchel, M.; Brudanin, V.; Caffrey, A.; Cailleret, J.; et al. Technical design and performance of the NEMO 3 detector. *Nuclear Instruments and Methods in Physics Research Section A: Accelerators, Spectrometers, Detectors and Associated Equipment* **2005**, *536*, 79–122.
6. Hamamatsu Photonics. *Hamamatsu R6091 Photomultiplier Tube*, 2016. TPMH1114E04, https://www.hamamatsu.com/resources/pdf/etd/R6091_TPMH1114E.pdf.
7. Cockcroft, J.D.; Walton, E.T. Experiments with high velocity positive ions. *Proceedings of the Royal Society of London. Series A, containing papers of a mathematical and physical character* **1930**, *129*, 477–489.
8. Katz, U.; et al. Status of the KM3NeT project. *Nuclear Instruments and Methods in Physics Research Section A: Accelerators, Spectrometers, Detectors and Associated Equipment* **2009**, *602*, 40–46.
9. Adrian-Martinez, S.; Ageron, M.; Aharonian, F.; Aiello, S.; Albert, A.; Ameli, F.; Anassontzis, E.; Andre, M.; Androulakis, G.; Anghinolfi, M.; et al. Letter of intent for KM3NeT 2.0. *Journal of Physics G: Nuclear and Particle Physics* **2016**, *43*, 084001.
10. Gajanana, D.; Gromov, V.; Timmer, P. ASIC design in the KM3NeT detector. *Journal of Instrumentation* **2013**, *8*, C02030.
11. Real, D.; Calvo, D. Digital Optical Module Electronics of KM3NeT. *Physics of Particles and Nuclei* **2016**, *47*, 918–925. <https://doi.org/10.1134/S1063779616060216>.
12. Information technology — Generic cabling for customer premises. standard 11801, International Organization for Standardization, International Electrotechnical Commission, 2017.
13. Aiello, S.; Albert, A.; Alshamsi, M.; Garre, S.A.; Aly, Z.; Ambrosone, A.; Ameli, F.; André, M.; Androulakis, G.; Anghinolfi, M.; et al. Nanobeacon: A time calibration device for the KM3NeT neutrino telescope. *Nuclear Instruments and Methods in Physics Research Section A: Accelerators, Spectrometers, Detectors and Associated Equipment* **2022**, *1040*, 167132.
14. Huber, T.; Kelley, J.; Kunwar, S.; Tosi, D.; Collaboration, I.G.; et al. The IceTop scintillator upgrade. In Proceedings of the 35th International Cosmic Ray Conference. SISSA Medialab, 2018, Vol. 301, p. 401.
15. IRIG Serial Time Code Formats. standard 200-04, Telecommunications and Timing Group, Range Commanders Council, U.S. Military, 2004.
16. Evans, J.M.; O'Neill, J.T.; Little, J.L.; Albus, J.S.; Barbera, A.J.; Fife, D.W.; Fong, E.N.; Gilsinn, D.E.; Holberton, F.E.; Lucas, B.G.; et al. Standards for computer aided manufacturing. interim report NBSIR 76-1094 (R), National Bureau of Standards, U.S. Department of Commerce, 1976.
17. SeedStudio BeagleBone® Green. <https://www.beagleboard.org/boards/seedstudio-beaglebone-green>.
18. Lipiński, M.; Włostowski, T.; Serrano, J.; Alvarez, P. White Rabbit: A PTP application for robust sub-nanosecond synchronization. In Proceedings of the 2011 IEEE International Symposium on Precision Clock Synchronization for Measurement, Control and Communication. IEEE, 2011, pp. 25–30.
19. IEEE Standard for a Precision Clock Synchronization Protocol for Networked Measurement and Control Systems. *IEEE Std 1588-2019 (Revision of IEEE Std 1588-2008)* **2020**, pp. 1–499. <https://doi.org/10.1109/IEEESTD.2020.9120376>.
20. Oehler, E. Long Distance White Rabbit High Accuracy time over fiber link. Technical report, Safran Navigation & Timing, 2023. <https://safran-navigation-timing.com/long-distance-white-rabbit-high-accuracy-time-over-fiber-link/>.
21. White Rabbit Switch open hardware repository. <https://ohwr.org/projects/white-rabbit/wiki/switch>.
22. White Rabbit CHROMIUM Switch. <https://redmine.nikhef.nl/et/projects/chromium/wiki/Backplane-20SFP>.
23. White Rabbit Switch with Low Jitter daughterboard (WRS-LJ). <https://creotech.pl/product/white-rabbit-switch-with-low-jitter-daughterboard-wrs-lj/>.
24. Seven Solutions. *White Rabbit LEN*, 2019. <https://sevensols.com/home/timing-products/wr-len/>.
25. Aiello, S.; Ameli, F.; Andre, M.; Androulakis, G.; Anghinolfi, M.; Anton, G.; Ardid, M.; Aublin, J.; Bagatelas, C.; Barbarino, G.; et al. KM3NeT front-end and readout electronics system: hardware, firmware, and software. *Journal of Astronomical Telescopes, Instruments, and Systems* **2019**, *5*, 046001–046001.
26. Bendfelt, T.; Kelley, J.; Mánek, P.; et al. MicroDAQ CHIPS repository. <https://github.com/WIPACrepo/microdaq-chips>, 2019.
27. Bash, S.; Cesar, J.; Deuerling, G.; Dodwell, T.; Germani, S.; Mánek, P.; Niner, E.; Norman, A.; Thomas, J.; Tingey, J.; et al. Low-latency NuMI trigger for the CHIPS-5 neutrino detector. *Nuclear Instruments and Methods in Physics Research Section A: Accelerators, Spectrometers, Detectors and Associated Equipment* **2022**, *1030*, 166513.
28. Tingey, J.; Mánek, P.; Germani, S.; et al. CHIPS DAQ repository. <https://gitlab.com/chipsneutrino/chips-daq>, 2019.
29. Patterson, D.A.; Gibson, G.; Katz, R.H. A case for redundant arrays of inexpensive disks (RAID). In Proceedings of the Proceedings of the 1988 ACM SIGMOD international conference on Management of data, 1988, pp. 109–116.
30. CentOS Linux 7. <https://centos.org/centos-linux/>.
31. System and Service Manager. <https://systemd.io/>.
32. Elasticsearch: The Official Distributed Search & Analytics Engine. <https://www.elastic.co/elasticsearch>.
33. ELK Stack: Elasticsearch, Kibana, Beats & Logstash. <https://www.elastic.co/elastic-stack>.
34. Kibana: Explore, Visualize, Discover Data. <https://www.elastic.co/kibana>.
35. Burri, A.; Gerhardt, M. TinyFSM: A simple C++ finite state machine library. <https://github.com/digint/tinyfsm>, 2012.
36. D'Amore, G.; et al. nanomsg-next-generation – light-weight brokerless messaging. <https://github.com/nanomsg/nng>, 2016.
37. Brun, R.; Rademakers, F. ROOT—An object oriented data analysis framework. *Nuclear instruments and methods in physics research section A: accelerators, spectrometers, detectors and associated equipment* **1997**, *389*, 81–86.
38. Kohlhoff, C. Boost.Asio. https://www.boost.org/doc/libs/1_66_0/doc/html/boost_asio.html, 2017.

39. Cormen, T.H. *Introduction to Algorithms, 3rd Edition*; The MIT Press, 2009.
40. Knuth, D.E. *The Art of Computer Programming: Volume 3: Sorting and Searching (2nd Edition)*; Addison-Wesley Professional, 1998.
41. Pordes, R.; Petravick, D.; Kramer, B.; Olson, D.; Livny, M.; Roy, A.; Avery, P.; Blackburn, K.; Wenaus, T.; Würthwein, F.; et al. The Open Science Grid status and architecture. In *Proceedings of the Journal of Physics: Conference Series*. IOP Publishing, 2008, Vol. 119, p. 052028.
42. Blake, A.; Germani, S.; Pan, Y.; Perch, A.; Pfützner, M.; Thomas, J.; Whitehead, L. CHIPS event reconstruction and design optimisation. *arXiv preprint, arXiv:1612.04604* **2016**.
43. Dealtry, T.; et al. The WCSim GEANT4 application. <https://github.com/WCSim/WCSim>, 2014.
44. Perch, A.; Whitehead, L.; Tingey, J.; Pfützner, M.; et al. CHIPS Simulation repository. <https://gitlab.com/chipsneutrino/chips-sim>, 2019.
45. Perch, A.; Whitehead, L.; Tingey, J.; Pfützner, M.; et al. CHIPS Event Reconstruction repository. <https://gitlab.com/chipsneutrino/chips-reco>, 2019.
46. Andreopoulos, C.; Bell, A.; Bhattacharya, D.; Cavanna, F.; Dobson, J.; Dytman, S.; Gallagher, H.; Guzowski, P.; Hatcher, R.; Kehayias, P.; et al. The GENIE neutrino Monte Carlo generator. *Nuclear Instruments and Methods in Physics Research Section A: Accelerators, Spectrometers, Detectors and Associated Equipment* **2010**, *614*, 87–104.
47. Hagmann, C.; Lange, D.; Wright, D. Monte Carlo simulation of proton-induced cosmic ray cascades in the atmosphere. Technical report, Lawrence Livermore National Laboratory, Livermore, CA (United States), 2007.
48. Agostinelli, S.; Allison, J.; Amako, K.a.; Apostolakis, J.; Araujo, H.; Arce, P.; Asai, M.; Axen, D.; Banerjee, S.; Barrand, G.; et al. GEANT4—a simulation toolkit. *Nuclear instruments and methods in physics research section A: Accelerators, Spectrometers, Detectors and Associated Equipment* **2003**, *506*, 250–303.
49. Mukhopadhyay, P.; Chaudhuri, B.B. A survey of Hough Transform. *Pattern Recognition* **2015**, *48*, 993–1010.
50. Tingey, J.; Bash, S.; Cesar, J.; Dodwell, T.; Germani, S.; Kooijman, P.; Mánek, P.; Ozkaynak, M.; Perch, A.; Thomas, J.; et al. Neutrino characterisation using convolutional neural networks in CHIPS water Cherenkov detectors. *Journal of Instrumentation* **2023**, *18*, P06032.
51. Simonyan, K.; Zisserman, A. Very deep convolutional networks for large-scale image recognition. *arXiv preprint, arXiv:1409.1556* **2014**.

Disclaimer/Publisher’s Note: The statements, opinions and data contained in all publications are solely those of the individual author(s) and contributor(s) and not of MDPI and/or the editor(s). MDPI and/or the editor(s) disclaim responsibility for any injury to people or property resulting from any ideas, methods, instructions or products referred to in the content.